Article:
Mikula, R. orcid.org/0009-0004-4283-4131, Sternovsky, Z., Armes, S.P. orcid.org/0000-0002-8289-6351 et al. (11 more authors) (2024) Impact ionization mass spectra of polypyrrole-coated anthracene microparticles: a useful mimic for cosmic polycyclic aromatic hydrocarbon dust. ACS Earth and Space Chemistry, 8 (3). pp. 586-605. ISSN 2472-3452

https://doi.org/10.1021/acsearthspacechem.3c00353

Impact Ionization Mass Spectra of Polypyrrole-Coated Anthracene Microparticles: A Useful Mimic for Cosmic Polycyclic Aromatic Hydrocarbon Dust

R. Mikula,[1,2] Z. Sternovsky,[1,2] S. P. Armes,[3] E. Ayari,[1,4] J. Bouwman,[1,5] D. H. H. Chan,[3] M. Horanyi,[1,4] J. K. Hillier,[6] S. Kempf,[1,5] N. Khawaja,[6] Z. Kupihár,[7] F. Postberg,[6] and R. Srama[8]

[1] *Laboratory for Atmospheric and Space Physics, University of Colorado, Boulder 80303, USA*

[2] *Smead Aerospace Engineering Sciences Department, University of Colorado, Boulder 80303, USA*

[3] *Dainton Building, Department of Chemistry, University of Sheffield, Brook Hill, Sheffield, South Yorkshire, S3 7HF, UK*

[4] *Department of Physics, University of Colorado, Boulder 80303, USA*

[5] *Department of Chemistry, University of Colorado, Boulder 80303, USA*

[6] *Institute of Geological Sciences, Frei Universität Berlin, 12249 Berlin, Germany*

[7] *Department of Medical Chemistry, University of Szeged, H-6720 Szeged, Hungary*

[8] *Institute for Space Systems, Stuttgart University, 70569 Stuttgart, Germany*

Abstract

Polycyclic aromatic hydrocarbons (PAHs) are abundantly present in the interstellar medium and in our solar system and lock up a significant fraction of cosmic carbon. They are found to be present in interstellar and interplanetary dust particles. Impact ionization mass spectrometers on future space missions can detect such dust particles and assess their composition; it is essential to understand the impact ionization behavior of PAH-based dust particles impinging on metal targets at relevant velocities. To date, impact ionization studies of fast-moving organic-rich dust particles have been limited to vinyl polymers such as polystyrene or poly(methyl methacrylate). Recently, the PAH anthracene has been prepared in the form of microparticles suitable for use in dust accelerators. Here we present the first comprehensive study of the impact ionization mass spectra of such anthracene microparticles impinging on a gold target at 2 – 35 km s^{-1}. The mass spectra recorded for the resulting ionic plasma are strongly dependent on the incident velocity, with impacts at 6 – 10 km s^{-1} being optimal for generating distinctive spectral features that enable the identification of the parent molecule. Under these conditions, the protonated parent ion and doubly protonated radical, $C_{14}H_{11}^{+}$, and $C_{14}H_{12}^{\cdot +}$, (as well as other diagnostic cluster species such as $(C_{14}H_{10})(CH)^{+}$ and $(C_{14}H_{11})(C_2H)^{+}$) can be reproducibly identified. We find that the impact ionization spectra always differ markedly from the electron impact ionization mass spectra reported for anthracene in the literature, regardless of the impact velocity. This study highlights the importance of performing fundamental impact ionization studies of organic particles using a dust accelerator to enable the interpretation of data collected in future space missions.

1. Introduction

Polycyclic Aromatic Hydrocarbons (PAHs) comprise a family of organic molecules that are abundant in many interstellar sources, as evidenced by the characteristic mid-infrared emission bands arising from excitation by the interstellar radiation field [*Allamandola et al.* 1985; *Leger and Puget*, 1984; *Allamandola et al.* 1989]. PAHs have been observed in both reflection nebulae and extragalactic sources [*Tielens*, 2008; *Chiang & Ménard*, 2019]. Their infrared features are prominent in protoplanetary disks [*Seok & Li* 2017], signifying their presence during all stages of star formation. PAHs have also been identified within planetary atmospheres [*Zhao et al.* 2018] and are ubiquitously found in and around objects in our solar system [*Raman et al.* 2020]. For example, the Stardust mission studied the Jupiter Family Comet 81P/Wild2 and collected cometary dust grains within aerogel targets for detailed analysis [*Brownlee, et al*. 2004]. Two-step laser mass spectrometry and analysis indicated that these returned samples contained PAHs [*Clemett, et al.* 2010]. PAHs also comprise a large fraction of the organic species found in Interplanetary Dust Particles (IDPs) [*Allamandola et al.* 1987].

Impact ionization occurs when dust particles impinge on a solid (typically metal) target at high velocity ($v > 1$ km s^{-1}). The resulting ionic plasma can be analyzed using Time-of-Flight (ToF) mass spectrometry and is characteristic of the original dust particles. The Cosmic Dust Analyzer (CDA) on the Cassini spacecraft [*Srama et al.* 2004] contained an impact ionization dust analyzer. CDA collected thousands of mass spectra, including those originating from impinging IDPs and interstellar dust (ISD) particles [*Hiller et al.* 2009; *Altobelli et al.* 2016]. CDA was able to identify various classes of IDPs and ISDs, but the presence of organic species has never been confirmed. This is in part due to insufficient mass resolution ($m/\Delta m \leq 50$) for the analysis of organic species. The upcoming IMAP (Interstellar Mapping and Acceleration Probe [*McComas et al.* 2018] and DESTINY+ (Demonstration and Experiment of Space Technology for INterplanetary voYage with Phaethon fLyby and dUst Science (DESTINY+) [*Ozaki et al.* 2021] space missions will carry next-generation dust analyzer instruments with larger dust detection areas (≥ 500 cm^2 *and* ≥ 250 cm^2, respectively). These instruments will analyze the chemical composition of impinging dust particles after impact ionization and their reflectron-like ion optics will provide significantly higher mass resolution ($m/\Delta m \geq 100$). Such features are essential for the collection and analysis of organic species present in IDPs and ISD

particles due to their relatively low flux and complex nature. The presence of PAHs has been confirmed in various objects in our solar system through IR, UV, and optical observations. Future space missions will provide unique opportunities for the *in-situ* verification of complex organic molecules within cosmic dust grains.

Impact ionization differs from more conventional methods of ionization used in mass spectrometry. Various studies have documented the impact ionization properties of silicates and other minerals for impact velocities of up to tens of km s^{-1} [*Fiege et al.* 2014; *Hillier et al.* 2012; 2014; 2018]. However, the impact ionization studies of organic projectiles has been limited to polystyrene and aliphatic poly(methyl methacrylate) latex [*Goldsworthy et al.* 2002; 2003; *Srama et al.* 2009; *Burchell & Armes,* 2011]. The latter polymer is solely aliphatic, while the former polymer contains both aliphatic and aromatic bonds, so neither are satisfactory synthetic mimics for PAH dust grains. The wholly aromatic character of PAHs should mean that higher impact energies are required to break chemical bonds and distinctive molecular fragments are anticipated in their mass spectra [*Goldsworthy et al.* 2003; *Srama et al.* 2009; *Burchell & Armes,* 2011, *Hrodmarsson et al.* 2022, *Hrodmarsson et al.* 2023]. This article describes the first study of the impact ionization behavior of a suitable synthetic mimic for PAH-based dust grains. Alternative analytical methods such as electrospray, chemical ionization, and electron impact ionization (followed by laser dissociation) do not provide comparable data to that obtained in dust impact ionization experiments because the chemical composition of the resulting ionic plasma is strongly dependent on the impact velocity. Given the inherent variability between impact ionization events, it is critical that many experiments be performed over a wide velocity range to obtain statistically significant results.

We have studied the impact ionization mass spectra recorded when firing anthracene ($C_{14}H_{10}$) microparticles at a gold target for impact velocities ranging from 2 to 35 km s^{-1}. This range was selected because it is relevant for sampling IDPs by the IMAP and DESTINY+ missions and future missions to planetary systems; it also partially covers the velocity range expected for ISD particles. Particular attention is paid to how the relative abundances of cationic species vary with impact velocity. Primarily, we seek to characterize the distinctive molecular fragments and clusters that are formed as a function of impact velocity. Such spectral features should be beneficial in identifying anthracene (and other PAH species) using upcoming dust impact mass spectrometers such as IDEX.

2. Measurements

2.1. Anthracene Dust Sample

The preparation and characterization of the anthracene microparticles used in this study has been described in detail elsewhere [*Chan et al.* 2021]. Briefly, coarse anthracene crystals (97% purity) were ground into micrometer-sized particles using a planetary ball mill in the presence of a commercial anionic water-soluble polymer (Morwet D425). After purification to remove excess dispersant, the microparticles were coated with a ~20 nm overlayer of polypyrrole (PPy) using a well-known aqueous deposition protocol [*Chan et al.* 2021]. This electrically conductive coating allows the microparticles to acquire surface charge and thus enables their acceleration up to high velocities using an electrostatic accelerator. The particle size distribution of the polypyrrole-coated anthracene microparticles was assessed using laser diffraction, which indicated a volume-average particle diameter of approximately 4 µm. However, the size distribution is relatively broad and extends to the sub-micron range. Scanning electron microscopy (SEM) studies revealed that these microparticles are rather irregular in shape (Fig. 1).

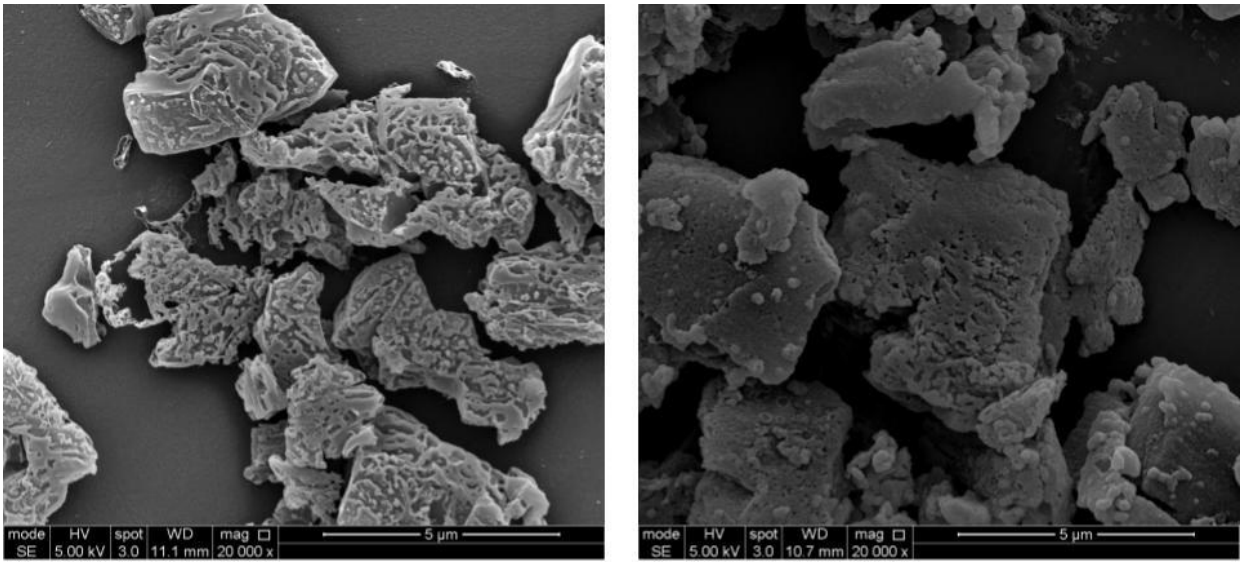

Figure 1. Representative SEM images showing the morphology of ~4 µm (and smaller) anthracene microparticles before (left) and after (right) coating with a 20 nm overlayer of polypyrrole (PPy). See main text for further details.

2.2. Accelerator Measurements

The measurements were performed using the dust accelerator facility operated at the University of Colorado [*Shu et al.* 2012]. An electrostatic potential of up to 3 MV is used for the acceleration of positively charged particles to speeds of tens of km/s. The dust sample is loaded into a reservoir installed at the high-voltage terminal. The reservoir is pulsed between 0 and 20 kV with respect to a sharp tungsten needle at 20 kV mounted within the reservoir, which results in the electrostatic lofting of the dust particles. Random collisions of the dust particles with the electrically biased needle confer cationic surface charge and they are then extracted from the dust source for subsequent acceleration. Pick-up tube detectors installed on the beamline are used to measure the velocity (v) and charge (q) of individual particles. The particle mass (m) and spherical equivalent radius (a) are calculated using $m = 2qU/v^2$, and $a = (3m/4\pi\rho)^{1/3}$, respectively. An acceleration voltage of $U = 2.2$ MV is used for all measurements described below. The mass density of the anthracene is $\rho = 1.25\ gcm^{-3}$and the contribution from the ultrathin PPy coating ($\rho \sim 1.50\ gcm^{-3}$) is neglected when calculating the particle radius (a). The accelerator facility is equipped with the Particle Selection Unit (PSU) subsystem that allows down-selecting of particles to the desired velocity and/or mass ranges using an electrostatic gate [*Mocker et al.* 2011; *Thomas et al.* 2013]. Passing the PSU, the particles travel along the beam

line into the main vacuum chamber. Before entering this chamber, an additional pick-up tube detector is used to verify the arrival of the particles and to confirm their velocity and mass. The temporal variation of the induced charge signal (QD) from the last pick-up tube detector is recorded for each impact event along with the mass spectra.

The anthracene sample is mixed with coarser iron dust in about a 1:1 mass ratio. This common practice improves the performance of the dust source for samples that are poorer conductors than metals. Due to their larger size (6 to 10 μm), the iron particles are accelerated to less than 1 km s^{-1} and are consequently readily eliminated using the PSU. The accelerator beamline and the experimental chamber are evacuated to pressures below 10^{-7} Torr and 10^{-6} Torr, respectively.

2.3 IDEX Prototype Instrument

The impact ionization mass spectra are collected by the laboratory prototype version of the Interstellar Dust Experiment (IDEX) instrument installed in the vacuum chamber at the end of the beamline. IDEX is currently in development for flight onboard the IMAP mission [*McComas et al.* 2018]. The prototype instrument has the same form factor, similar ion optics design, and target as the flight version of IDEX in development and is expected to achieve similar levels of performance.

IDEX is an impact ionization ToF mass spectrometer developed for space applications and is a result of a series of maturation efforts reported by [*Rachev et al.* 2004]; *Srama et al.* 2005; and *Sternovsky et al.* 2007, 2011, 2015]. The heritage instrument is the CDA that operated onboard the Cassini spacecraft [*Srama et al.* 2004]. In comparison to CDA, IDEX provides a larger target area in combination with a higher mass resolution, which makes its design suitable for the detection and analysis of interstellar and interplanetary dust particles [*Grün et al.* 2005].

The ion optics consist of a target plate, an acceleration grid, a set of ring electrodes, and a parabolic grid electrode. The target, where dust impacts occur, is of annular shape with a 40 cm outer diameter and is biased at +3.0 kV. The cations from the impact plasma are extracted by the grounded acceleration grid that is placed 3 cm above the target. The electrically biased ring electrodes and parabolic grid provide a reflectron-like focusing of the ions onto a centrally located ion detector. For more details on the design of the ion optics see [*Sternovsky et al.* 2015]. The mass resolution of the instrument is $m/dm > 100$ at mass $m = 100$ u. The ion detector is

an in-house developed discrete dynode electron multiplier with a sensitive area of 40 mm in diameter. The width of the output pulse from a single particle detection is about 15 ns (FWHM), which is sufficiently fast for the instrument of this size, and does not significantly broaden the measured mass lines, or affect mass resolution. The detector output is directly connected to the input of a fast, multichannel digitizing scope with a 50 ohm termination, 200 MHz bandwidth, and data acquisition rate of 500 MSs^{-1}. The data acquisition is triggered using the signal from the detector, i.e. the first mass line with an amplitude over the preset threshold triggers the data acquisition and is assigned $t = 0$ in the data set. The scope records a pre- and post-trigger time window of approximately –900 ms to 100 ms and includes the recording of the QD detector signal. The QD detector is located approximately 1.97 m upstream from the impact target.

The target of the IDEX prototype instrument is assembled from six equal segments that are machined out of aluminum and plated with nickel. The target segment used for the measurements is polished to an rms surface roughness of less than 5 nm and coated with a 1 μm thick high-purity gold layer using a magnetron sputtering machine. Gold is selected as the target material for its high mass density, cleanliness, and high atomic mass that does not interfere with the more common elements expected to appear in the acquired mass spectra.

2.4 Particle Size Distribution

Impact ionization mass spectra were collected over a duration of four days. The PSU was set to allow particles travelling at 2 km s^{-1} or more to reach the detector for most of the measurements. On the final day of the campaign, the velocity limitation was set to > 10 km s^{-1} to increase the fraction of mass spectra recorded at higher velocities. In total, 1884 spectra were collected, of which 1667 were judged to be of sufficiently good quality for further analysis (Fig. 2). The remaining 217 recorded events either had ambiguities in their particle mass or velocity, or the mass spectra were judged to be of inferior quality. The latter were attributed to dust particles striking one of the grids in the instrument before reaching the impact target, along with various non-target dust impacts. The velocities and masses for the 1667 particles ranged from 2.2 km s^{-1} to 34.1 km s^{-1} and from 10^{-18} to 10^{-14} kg (which corresponds to effective particle radii of approximately 40 nm to 700 nm). The velocity distribution of the particles is inversely correlated with their size distribution because higher velocities are only attained for smaller particles [*Shu et al.* 2012].

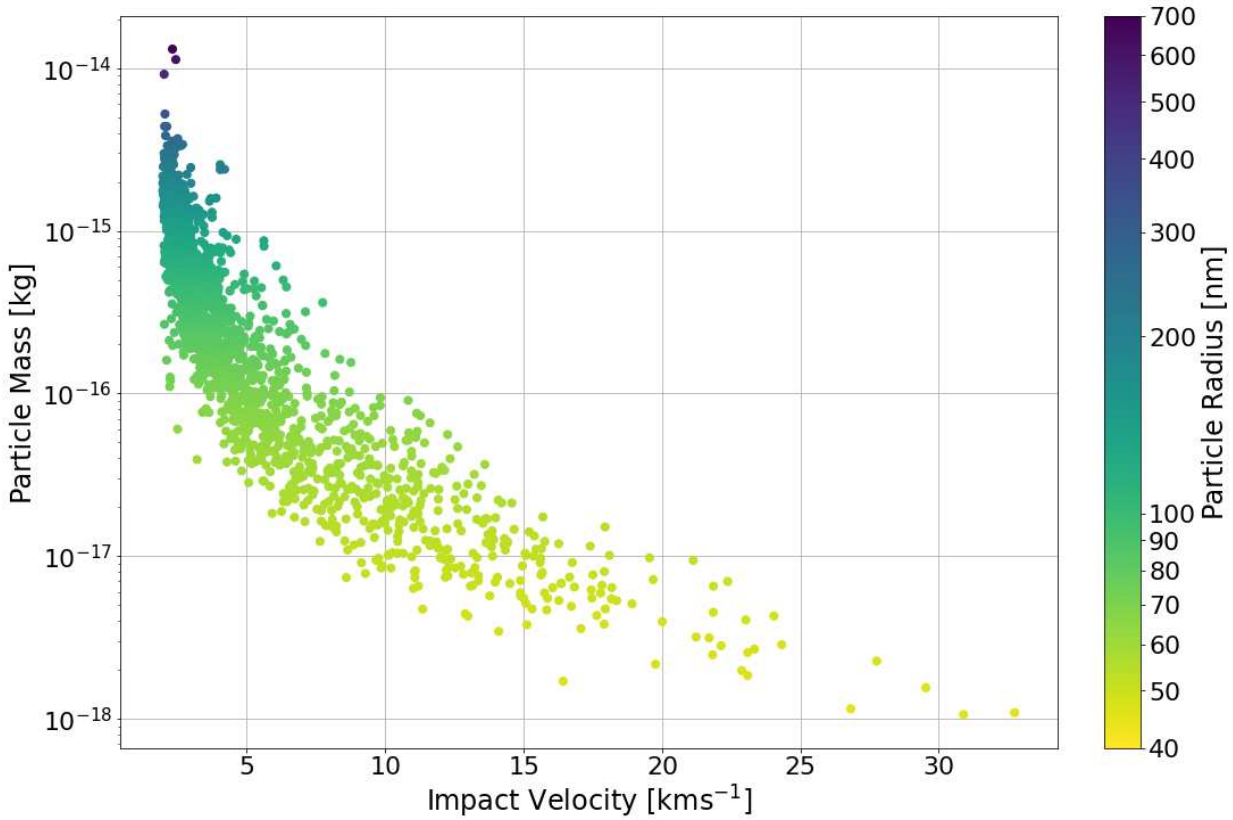

Figure 2. Mass [kg] vs. velocity [km s^{-1}] distribution of 1667 particles for which mass spectra were recorded. The color bar indicates particle radius [nm].

3. ToF Mass Spectra Analysis

3.1. Simplifying Assumptions

Several simplifying assumptions are made when analyzing the mass spectra. The first is that the velocity and angular distributions of ions are independent of the ion species in the expanding impact ionization plasma cloud. The ion optics of the IDEX prototype instrument focus only a fraction of ions onto the detector, preferentially those emitted with velocities close to the surface normal. The ion collection efficiency (i.e., ratio of ions that reach the detector) is estimated to be in the range of 10 to 50% and it is further assumed that the composition of these ions is the same as their global composition.

The next assumption is that all ions reaching the detector have the same probability of detection, regardless of their mass. This is a necessary simplifying assumption: the detection

efficiency is known to be lower for heavier ions [*Keifer et al.* 2017] but this reduction has not been characterized for the detector used in this study. Future flight instruments will most likely require the same assumption.

3.2. Data analysis

Data analysis was performed using an in-house software package called '*Spectrum*.' The first step involves processing the QD signals for each impact event to obtain the preliminary velocity v and mass m of each impinging particle. The software automatically identifies the time and amplitude of the signal arising from the particle as it enters and exits the pick-up tube detector [*Shu et al.* 2012]. These preliminary values are then compared with data collected by the PSU to obtain refined v and m values.

The data was then organized according to impact velocity and binned into twelve distinct ranges (Fig. 3). The analysis of complex organic mass spectra is time-intensive, so only a subset of thirty randomly selected spectra was analyzed in detail for each velocity bin. For bins containing fewer than 30 mass spectra, analysis was expanded to all available data in that bin.

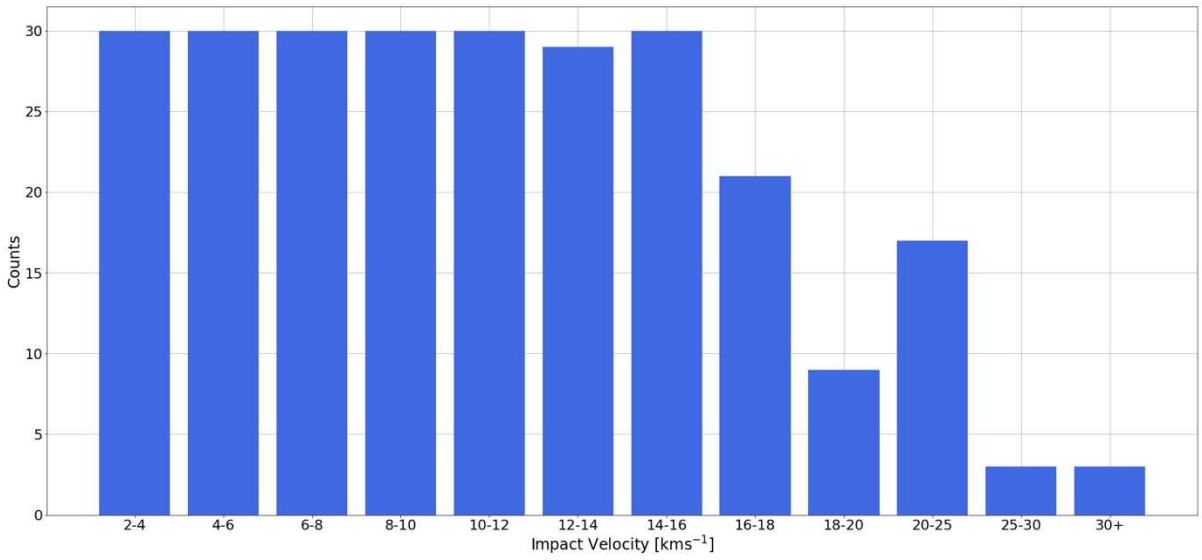

Figure 3. Number of randomly selected mass spectra analyzed in detail for each velocity bin.

The next step involves trimming the ToF signals: each event is imported with an initial time window $(-20, 40)$ µs with respect to the trigger time at $t = 0$. This ensures that the mass spectrum from the time of impact up to a mass line of at least $m = 300$ u is included in the data for further analysis. The ToF spectra are filtered and then baseline-corrected. Such filtering

reduces high frequency noise but does not affect the overall shapes and amplitudes of the mass lines. The baseline correction removes offset and low-frequency noise and improves the accuracy of calculating the ion content of the mass lines. Negative data points are set to the rms value of the signal noise, outside of the mass spectrum. This rms noise is also set as the baseline for calculating ion content. This processing allows the ToF data to be plotted on a logarithmic scale to aid identification of low-amplitude mass lines.

Analysis of the ToF mass spectra is performed in the time domain. First, prominent mass lines with signal-to-noise ratios (SNR) greater than 15 are identified. The detector gain and data acquisition are set up such that the dynamic range of the ToF measurements is greater than 100. Intense identifiable lines are used to establish the preliminary conversion between the time-of-flight and the corresponding ion mass using the relation $t = t_0 + \sqrt{\alpha m}$. Here m is the ion mass with units of atomic mass (u), α is the '*stretch parameter*' that is characteristic of the instrument geometry and applied bias voltages and varies slightly with impact location, while t_0 is the '*shift parameter*' that accounts for the time difference between the particle impact on the target and the triggering of the data acquisition (t_0 varies from impact to impact). Since the precise time of impact is not known, at least two mass lines are necessary to calculate preliminary numerical values for t_0 and α.

The mass spectra within each velocity bin are similar in terms of their most prominent mass lines. The presence of a dominant and unambiguous mass line (or anchor line) is helpful at the beginning of the analysis. This was usually Na^+ for impact velocities $v \leq 8$ km s^{-1} and H^+ for velocities $v > 12$ km s^{-1}. In the 8 – 12 km s^{-1} regime, either H^+ or Na^+ was used as the anchor line. spectral features identified beyond the anchor line can vary in their corresponding mass. A peak corresponding to a higher mass such as Au^+ or $C_{14}H_{10}^+$ is selected and assigned to the corresponding mass. This combined with the anchor line is used to find the best fit for the stretch parameter. The resulting stretch parameter for each spectrum ranged from $1.343\ \mu s \leq \alpha \leq 1.353\ \mu s$ because the target impact location varies slightly from impact to impact (the dust beam width is approximately 1 cm). A template of mass lines that frequently appear in the spectra was constructed as data analysis progressed. This template aided assignment of their correct mass. Finally, the relative abundance was calculated for all mass lines identified in each spectrum. Mass lines were fitted using either a Gaussian or an exponentially modified Gaussian to calculate

their ion content. Exponentially modified Gaussian fits were primarily used on species whose peak width skewed to the right, such as gold ions. The above parameters were refined and finalized as the data analysis progressed and further spectral lines were identified.

In cases of overlap between adjacent mass lines, the ion content is calculated iteratively for each mass: The fit of the first peak (lower mass) is subtracted from the signal such that the shape of the second peak (larger mass) can be calculated accurately. This protocol is followed from low to high mass across each spectrum. The ion content for each mass line is calculated as the area under the corresponding curve after performing the deconvolution using the iterative method described above. The total ion content is then calculated as the sum of all identified lines and assigned an area. Only minor mass lines that are (1) not reproducible within a velocity bin and (2) those with SNR ≤ 3 are omitted from this analysis. This approach accounts for more than 99% of the total ion content. The final tabulated output for each impact event provides the particle mass, size, and impact velocity, plus a list of all identified mass lines along with their relative contributions to the total ion content.

Corrections for the ^{13}C isotope effect are made using the known ^{13}C / ^{12}C ratio = 0.0108. The $C_nH_m^+$ features are clustered with $^{12}C_n$ being the lowest mass in each cluster. First-order corrections are calculated iteratively starting from low masses up to 184 u, following the scheme presented in Table 1. This means that we only consider the possibility of a single ^{13}C isotope in each molecular fragment. As expected, isotopic correction becomes more important for larger molecules (i.e. higher *n* values). After calculating the relative contributions for $^{12}C_nH_m^+$ and $^{13}C^{12}C_{n-1}H_m^+$, these are summed to obtain the absolute line area associated with each species: e.g., the absolute area for the $C_6H_2^{\cdot+}$ species is calculated as the contribution from $^{12}C_6H_2^{\cdot+}$ *plus* the contribution from $^{13}C^{12}C_5H_2^{\cdot+}$. This approach is flawed for mass features associated with $C_3H_3^+$ to $C_3H_8^+$ species owing to the appearance of K^+ and Ca^+ at 39 u, 40 u, and 41u. Fortunately, this problem is not important in practice because the mass lines assigned to $C_3H_3^+$, $C_3H_4^{\cdot+}$, $C_3H_5^+$, $C_3H_6^{\cdot+}$, $C_3H_7^+$, and $C_3H_8^{\cdot+}$ contribute less than 1% of the total ion content while mass lines associated with K^+ and Ca^+ contribute more than 10% of the total ion content at low impact speeds.

Table 1: Iterative algorithm for calculating the total ion content for C_nHm+ species in each hydrocarbon cluster with k = 0, 1, 2, … 'Mass Line' designates the mass line for which this

isotope correction was made. ‘Species 1’ and ‘Species 2’ denote the solely 12C species and its single 13C isotopologue respectively, while ‘Area 1’ and ‘Area 2’ represent their corresponding areal contributions to each spectral feature. The final column summarizes the total line area attributed to CnHm+ species.

k	Mass Line	Iso 1	Iso 2	$A_{n,k}$	$B_{n,k}$	Total Area of Species
0	12n	$^{12}C_n^+$	$^{12}C_{n-1}{}^{13}C^+$	$A_{n,0} = A(12n)$	$B_{n,0} = A_{n,0}\, Rn$	$A_{n,0} + B_{n,0}$
1	12n+1	$^{12}C_nH^+$	$^{12}C_{n-1}{}^{13}CH^+$	$A_{n,1} = A(12n + 1) - B_{n,0}$	$B_{n,1} = A_{n,1}\, Rn$	$A_{n,1} + B_{n,1}$
2	12n+2	$^{12}C_nH_2^+$	$^{12}C_{n-1}{}^{13}CH_2^+$	$A_{n,2} = A(12n + 2) - B_{n,1}$	$B_{n,2} = A_{n,2}\, Rn$	$A_{n,2} + B_{n,2}$
...		...	...	...	...	...
k	12n+k	$^{12}C_nHm+$	$^{12}C_{n-1}{}^{13}CHm+$	$A_{n,k} = A(12n + k) - B_{n,k-1}$	$B_{n,k} = A_{n,k}\, Rn$	$A_{n,k} + B_{n,k}$

After calculating the ion contents, the spectra within each velocity bin are co-added to obtain a holistic view of the average/most probable spectroscopic characteristics. This approach reduces variation between individual spectra within a given velocity bin and enables the effect of increasing the impact velocity to be more readily identified. The apparently poorer mass resolution observed for co-added spectra is the result of minor discrepancies in mass calibration between individual data sets.

3.4 Characterizing Target Contaminations

A separate campaign was conducted to characterize the state of the target surface using iron dust particles. TOF spectra were recorded for impact velocities ranging from 2 to 35 km s^{-1}, which overlaps with the experiments conducted with anthracene particles. During impact ionization, part of the target is also ionized, including any surface or bulk contaminants within the target. The gold used for coating the target has a purity of 99.99%, with known bulk impurities being Pt, Ca, Ag and Cu (in order of decreasing abundance). Gold ions only begin to appear in the mass spectra above 10 km s^{-1} with an initial relative abundance of 1% that increases at higher impact velocities. None of the impurities present in the target material were identified in any of the analyzed mass spectra. The target surface was cleaned and handled in a clean environment only, and the IDEX prototype instrument was stored under a dry nitrogen atmosphere in a sealed container when not in use. Nevertheless, some surface contamination of the gold target is unavoidable [*Postberg et al.* 2009].

The spectra are analyzed in the same fashion as described above. In addition to iron and various iron oxides, several additional mass lines appear in the spectra (Fig. 4). The most prominent of these are identified as Na^+, K^+ and Ca^+, which are commonly observed for all impact ionization mass spectra owing to their relatively low ionization potentials. Such contamination may originate from either the dust sample or from the target [*Auer and Sitte*, 1968]. An additional set of persistent mass lines are observed in the spectra over a wide velocity range (Fig. 4). Based on their mass patterns, these are assigned to the ionization of methanol, ethanol, and/or isopropyl alcohol, i.e., volatile organic solvents used for cleaning the instrument and/or other parts of the vacuum chamber. The corresponding mass lines are consistent with those reported for electron impact mass spectrometry [NIST]. For example, the electron ionization of ethanol using 70 eV electrons produces characteristic mass lines (in order of decreasing abundance) at 46, 31, 29, 27, 26, 25, and 19 m/z, which are consistent with contamination lines in Fig. 4 for impact speeds below approximately 15 km s^{-1}. At higher impact velocities, complete molecular dissociation occurs to form solely H^+ and C^+ ions.

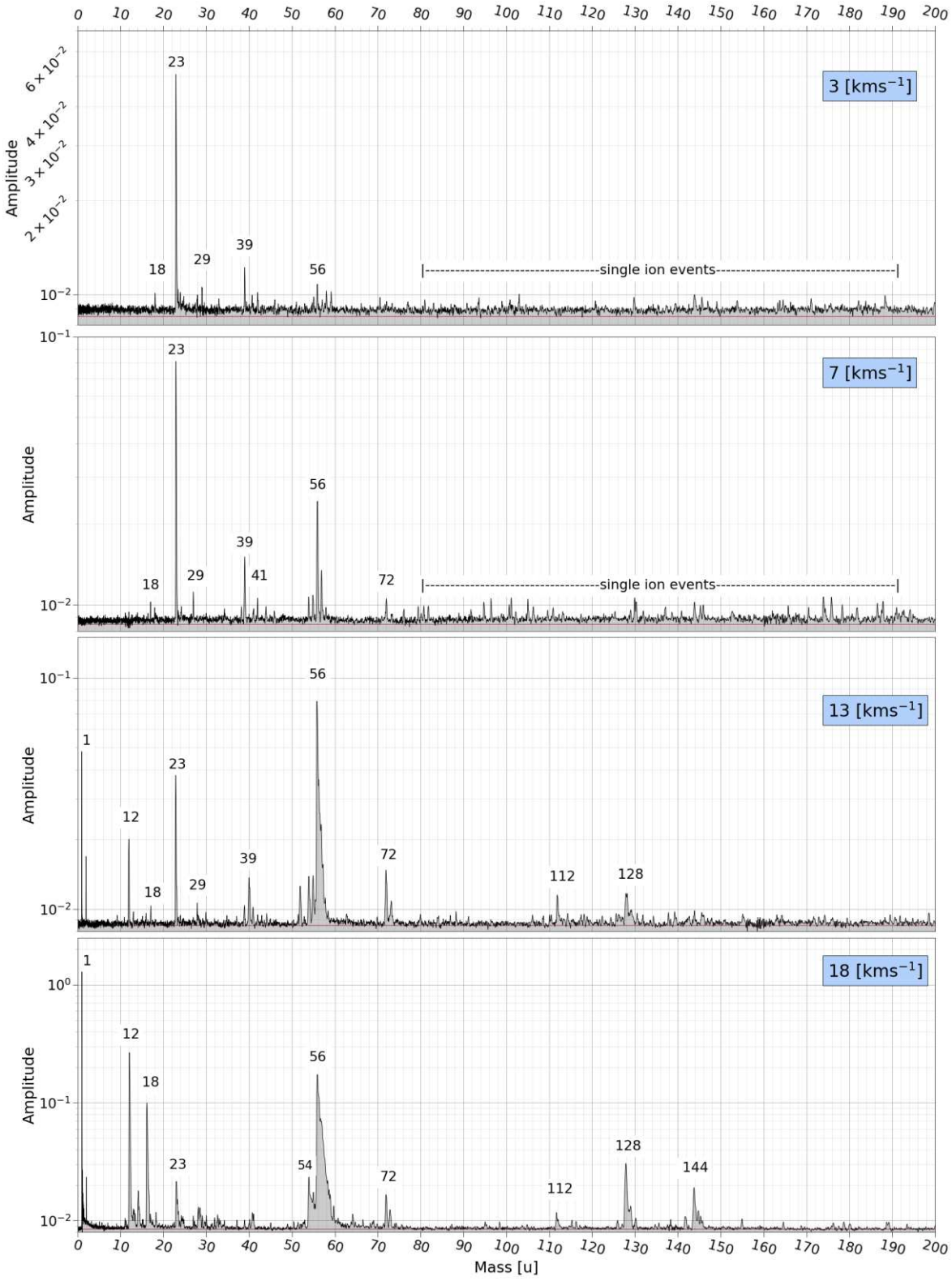

Figure 4. Representative impact ionization mass spectra recorded for individual iron dust impacts at 3, 7, 13, and 18 km s^{-1}. Characteristic mass lines assigned to iron isotopes ($^{54}Fe^{+}$ and

$^{56}Fe^+$) and iron oxide species such as FeO^+ (72u), Fe_2^+ (112u) and Fe_2O^+ (128 u) are labeled. The red line below each spectrum represents the signal baseline.

Each of the mass lines observed in Figure 4 can be assigned to either the dust particles or the (contamination on the) target surface. The pure hydrogen features (H^+, H_2^+, and H_3^+) become more prominent with increasing impact speed and are attributed to the combination of hydrogen adsorbed on the target surface [*Postberg et al.* 2009], plus the increasing fragmentation of other adsorbed molecules, including the alcohol contaminants discussed above. Hydrogen bonds strongly to metal surfaces and high-velocity impact ionization events provide sufficient kinetic energy for both dissociative ionization and the surface desorption of hydrogen atoms and molecules. Hydrogen ions are observed in every impact ionization mass spectrum above 15 km s^{-1} regardless of the dust composition [*Postberg et al.* 2009]. Carbon ions (12 u) arise from organic contaminants in the iron dust particles and on the target surface. In principle, contamination of the IDEX prototype may have occurred during its fabrication and handling. The presence of Na^+, K^+, and Ca^+ (which produce mass lines at 23, 39, 40, and 41 u) can be explained similarly.

The iron dust mass spectra also exhibit mass lines associated with water at 16, 17, 18 u (corresponding to O^+, OH^+, and $H_2O^{\cdot+}$, respectively). The most likely source of the OH^+ and $H_2O^{\cdot+}$ lines is surface-adsorbed water on either the target or the iron particles. Features associated with water and oxygen cations may stem from organic contaminants present on the target surface, as discussed previously. Mass lines assigned to FeO^+ (72 u), Fe_2O^+ (128 u), $Fe_2O_2^+$ (144 u) are the most prominent spectral features associated with the dust particles after the two Fe^+ mass lines (54/56 u). Thus, the O^+ species could in principle originate from the iron oxide surface layer on the dust particles.An additional mass line at 112 u assigned to Fe_2^+ is also observed for impact velocities above 6 km s^{-1}. Any mass lines originating from contaminants should be consistently seen between iron and anthracene spectra. In summary, the presence of contaminants is simply acknowledged, and their corresponding mass lines are excluded from the analysis.

4. Main Results and Discussion

4.1. Overview

Variation in the anthracene mass spectra with impact velocity led to the identification of four distinct velocity ranges corresponding to 2 – 6, 6 – 10, 10 – 16, and 16+ km s^{-1} (Fig. 5 and 6). For the lowest range, the most prominent mass line is the anthracene parent radical cation ($C_{14}H_{10}^{\cdot+}$) at 178 u and protonated anthracene ($C_{14}H_{11}^{+}$) at 179 u (it is important to note at this point that the 178 u mass feature can be attributed to any isomerization of $C_{14}H_{10}^{\cdot+}$, from this point forward, any mass at 178 u will be refferred to using $C_{14}H_{10}^{\cdot+}$). The latter is a combination of the protonated ion $C_{14}H_{11}^{+}$ and an isotopic species, $^{13}C^{12}C_{13}H_{10}^{\cdot+}$. Approximately 77% of the total ion content attributed to the 179 u mass line is related to $C_{14}H_{11}^{+}$ rather than its isotopologue $^{13}C^{12}C_{13}H_{10}^{\cdot+}$. This is important because it demonstrates that the ion content of this mass line is too large to be attributable to isotopic effects alone, thereby confirming the presence of protonated anthracene. In addition, the Na^{+} and K^{+} mass lines are prominent, as typically observed for low impact velocities. Mass lines at 191, 203, and 215 u are also important features in these low-velocity spectra; they represent clusters and are discussed at length in Section 4.3.

Spectra recorded in the 6 – 10 km s^{-1} range are similar in terms of their most prominent mass lines, but the relative abundance of the parent molecule is significantly lower. More importantly, a distinctive periodic hydrocarbon fragmentation pattern is observed from 60 u to 160 u. At 10 – 16 km s^{-1}, the parent ion is no longer present. Instead, hydrocarbon clusters begin to appear, starting at approximately 36 u; these clusters differ from those mentioned above and will be discussed in more detail in Section 4.3. Mass lines attributed to hydrogen (1, 2, and 3 u) and gold (197 u) are also consistently observed in this velocity range. Individual spectra (Fig. 6) contain mass lines occurring at almost every integer unit from 50 to 180 u, albeit often with much lower signal to noise (S/N) than that found for the characteristic $C_nH_m^{+}$ clusters. At higher impact velocities (16+ km s^{-1}), the mass features correspond almost entirely to $C_nH_m^{+}$ clusters with no evidence for the anthracene parent ion.

Here we briefly comment on the 56 u mass line that is consistently observed across all velocity ranges. This spectral feature cannot be attributed to the dissociative fragmentation of anthracene. In principle, it might correspond to $C_4H_8^+$. However, it does not appear in the electron ionization mass spectrum of anthracene [NIST]. Instead, this species most likely originates from the polypyrrole coating of the anthracene microparticles and is tentatively assigned to $C_3H_5NH^+$. It is not feasible to separate the majority of species coming from anthracene and PPy as they are both aromatic organic compounds. The large percentage of ion content coming from $C_{14}H_{10}{}^{\cdot+}$ and $C_{14}H_{11}^+$ cannot be generated from PPy, this indicates that the bulk of each spectrum obtained from PPy coated anthracene microparticles comes from the actual anthracene, not the coating. However, at higher impact velocities ($v > 16$ km s^{-1}), the bulk anthracene particles are significantly smaller (particle size is on the order of 60 – 100 nm including ~20 nm PPy overlayer) and contain more PPy coating relative to larger, slower particles (120 – 500 nm including ~20 nm PPy overlayer). This gives reason to be more cautious concerning the distinction of species origin and assignment at high impact velocities.

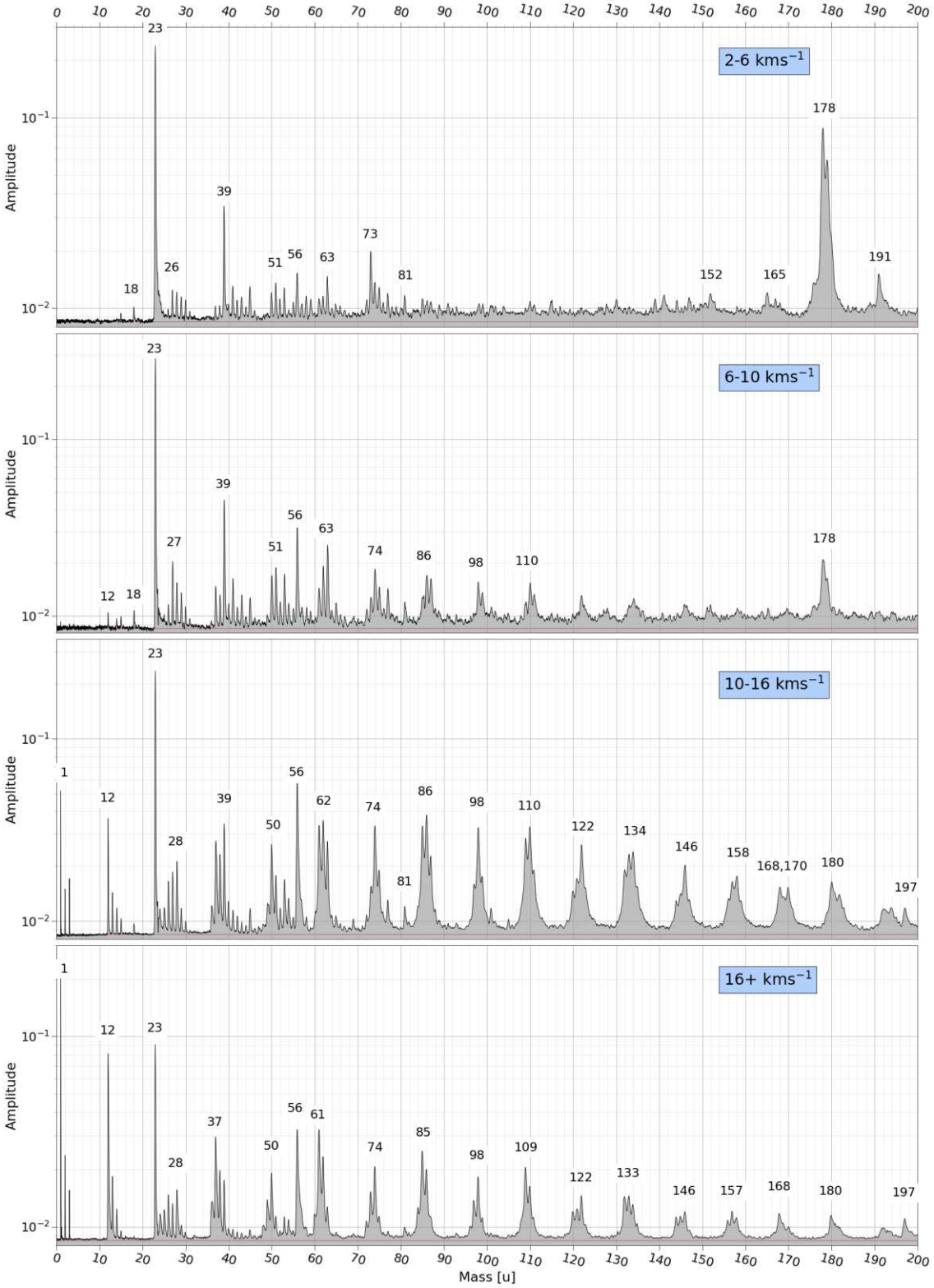
2-6 kms^{-1}
6-10 kms^{-1}
10-16 kms^{-1}
16+ kms^{-1}
Amplitude
Mass [u]

Figure 5. Co-added spectra recorded for anthracene particles for the following impact velocity ranges: 2 – 6, 6 – 10, 10 – 16, and 16+ km s^{-1} (from top to bottom). The anthracene parent ion appears at 178 and 179 u, while periodic hydrocarbon patterns are observed at 39, 50, 61, 74, 85, 98, 109, 122, 133, 146, 157 and 168 u in the form of $C_nH_m^+$. Mass lines at 23 and 39 u correspond to Na^+ and K^+ ion contaminants, respectively. See main text for further details.

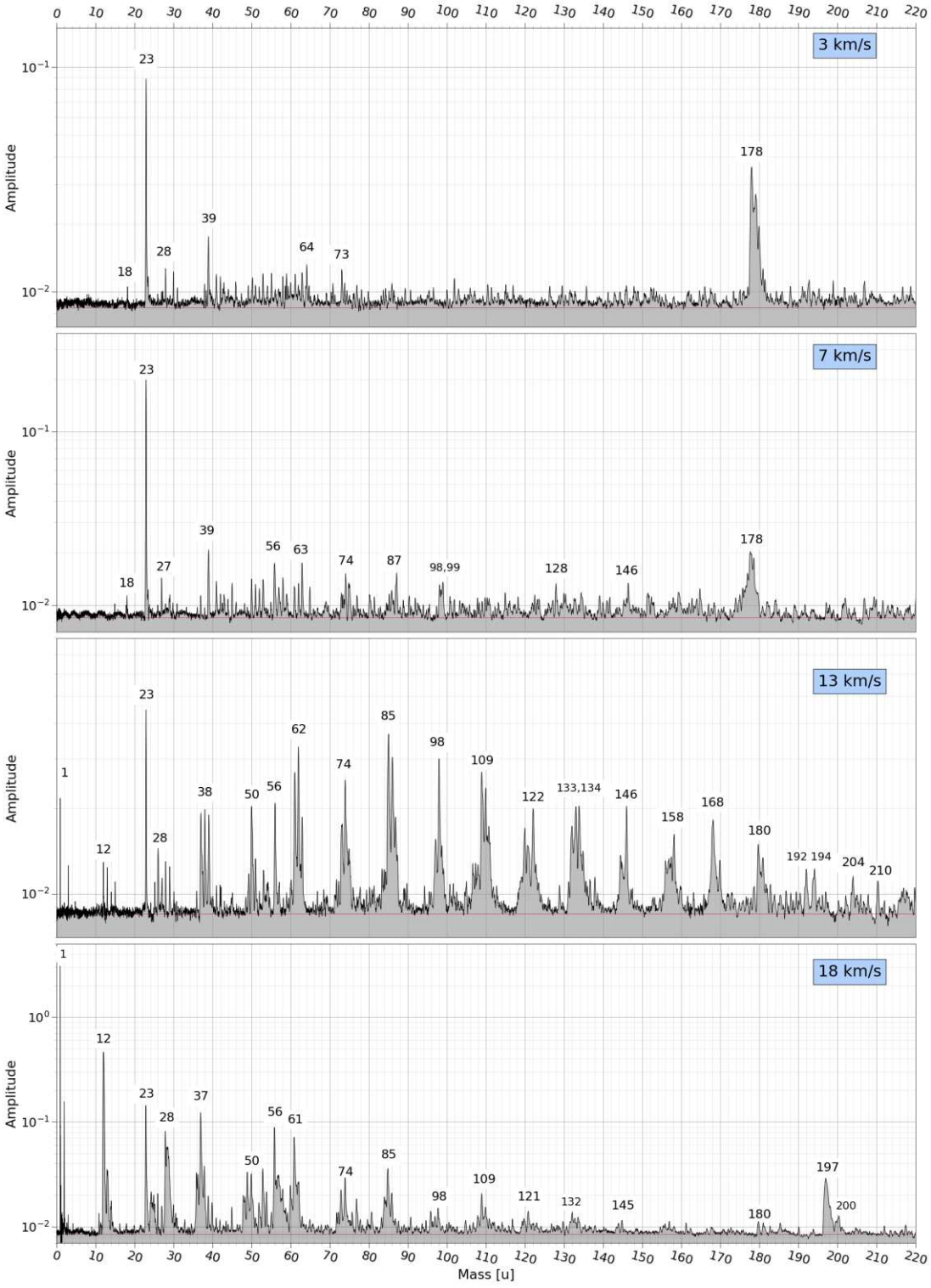

Figure 6. Representative individual mass spectra recorded for anthracene particles at impact velocities of 3, 7, 13, and 18 km s^{-1}, respectively (from top to bottom). See Fig. 5 caption and main text for further details.

4.2. Comparison with Electron Impact Ionization

Electron ionization (EI) is a common and well-established method in mass spectrometry for generating ionic species. Electron ionization occurs in the gas phase when a molecule interacts with a single high-energy (typically 70 eV) electron. The resulting molecular fragmentation pattern provides structural information. In contrast, dust impact ionization (DII) involves a high-energy impact between two solids (i.e., the particle and the target). For the 2 – 35 km s^{-1} impact velocity range investigated herein, the kinetic energy of the impinging particle varies from about 4 eV to more than 1.1 keV per anthracene molecule. This kinetic energy is sufficient to cause cratering of the target, melting and evaporation of the particle and target, and partial ionization of the evaporated species to form an ionic plasma. In this section, EI and DII mass spectra are critically compared [*Khawaja et al.* 2022] for anthracene.

Figures 7 and 8 show a comparison between the EI spectrum reported for anthracene in the literature and DII mass spectra recorded for the lower two velocity ranges, for which the parent ion is observed. Electron ionization of anthracene produces intense mass lines at 178, 152, 89, 76 and 63 u. Although there is some overlap between the mass lines produced by the two ionization methods, there are clear qualitative and quantitative discrepancies. At higher velocities, the DII spectra are extremely dissimilar with few to no overlapping features. Thus, there are fundamental differences in the molecular ionization processes involved in generating the EI and DII spectra. In summary, the existing database on electron ionization spectra cannot contribute to our understanding of laboratory-generated DII spectra for PAH-based synthetic particles or assist in the interpretation of DII spectra originating from PAH-rich dust impacts recorded by the IDEX and SUDA instruments in future space missions.

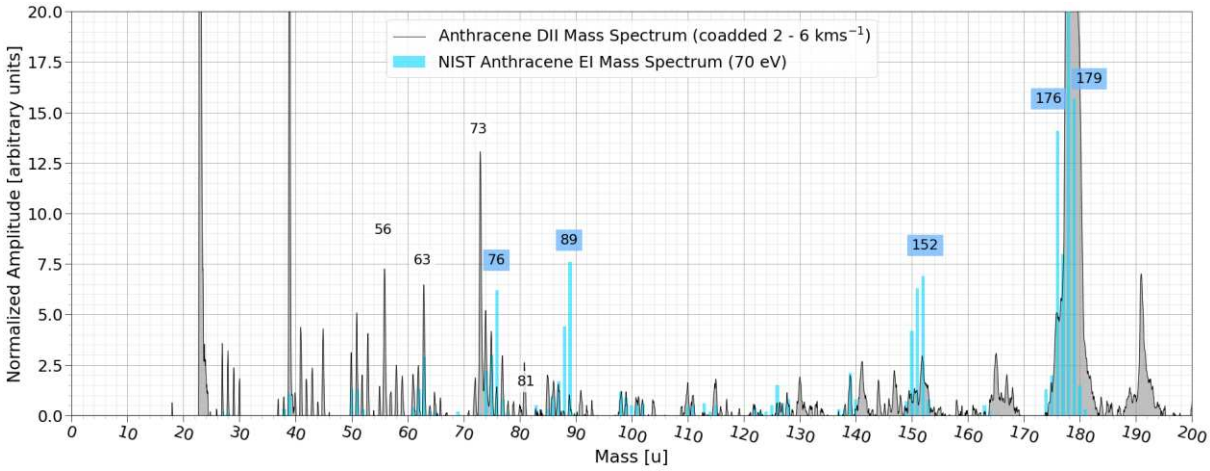

Figure 7. Comparison between the electron ionization mass spectrum recorded for anthracene (in blue) and the co-added spectrum originating from impact ionization using anthracene particles fired at 2 – 6 km s^{-1}. The mass spectra have been normalized by equating the amplitude of the largest line for each type of spectrum: Na^+ (23 u) for DII and the anthracene ion (178 u) are each set to a relative amplitue of 100 with a baseline of 0. The y-axis has been restricted on [0, 20] so that it is easier to visualize small peaks in both spectra.

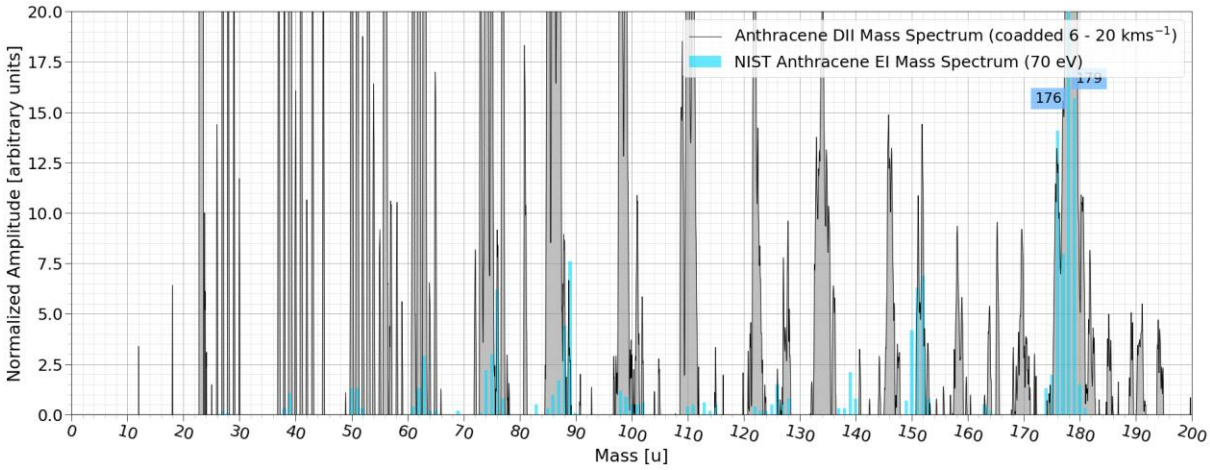

Figure 8. Comparison between the electron ionization mass spectrum recorded for anthracene (in blue) and the co-added spectrum originating from impact ionization using anthracene particles fired at 6 – 10 km s^{-1}. The mass spectra have been normalized by equating the amplitude of the largest line for each type of spectrum: The mass spectra have been normalized by equating the amplitude of the largest line for each type of spectrum: Na^+ (23 u) for DII and the anthracene ion (178 u) are each set to a relative amplitue of 100 with a baseline of 0. The y-axis has been restricted on [0, 20] so that it is easier to visualize small peaks in both spectra.

4.3. Evidence for Plasma Cloud Chemistry: Fragmentation Features versus Clustering

Throughout the velocity distribution, there are species that cannot be produced by the dissociation of anthracene alone. It then becomes crucial to explore how anthracene may fragment and how those fragmentation products may interact in the plasma cloud to form what we see as cationic clusters in the mass spectra. The conventional pathways for fragment loss in anthracene are C_2H_2 and C_4H_2 loss which then form biphenylene, cyclobuta[b]naphthalene, or naphthalene radical cations [*West et al.* 2014] (Fig. 9). The loss of C_2H_2 is the preferred pathway and is energetically favorable compared to the loss of C_4H_2, so we expect to see more features associated with C_2H_2 loss than C_4H_2 (152 u versus 128 u respectively). We see features at 152 u more prominently than at 128 u below 10 km s^{-1}, this indicates that the dissociative ionization pathways are likely similar between DII and the methods described in *West et al.* 2014 (Fig. 10).

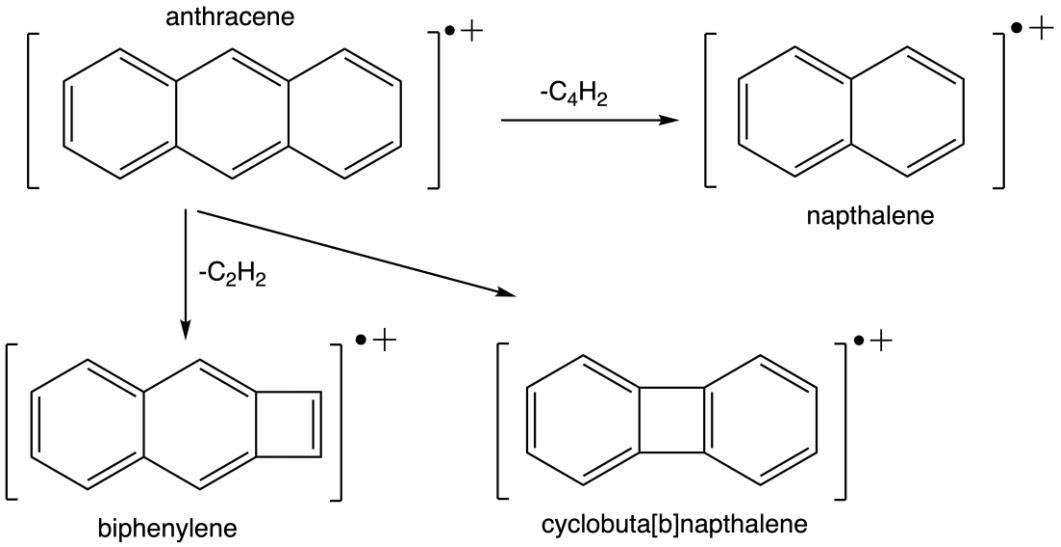

Figure 9. Dissociative ionization pathway for anthracene as measured using imaging photoelectron photoion coincidence spectrometry, which can lose C_2H_2 to form either biphenylene or cyclobuta[b]naphthalene or lose C_4H_2 to form naphthalene [*West et al.* 2014].

Above 10 km s^{-1}, a series of $C_nH_m^+$ species are observed that contain up to seventeen carbon atoms; the dissociation of anthracene ($C_{14}H_{10}$) alone cannot account for this observation. This confirms that some degree of chemistry and isomerization of molecular fragments must occur within the ionic plasma in this high-speed regime. Anthracene fragmentation should become more prevalent at higher impact velocities. This produces various molecular ions, protons, and neutral (radical) fragments such as C_2H_2, CH_2, C, and CH. As the concentration of such species increases within the plasma cloud, bimolecular chemistry will occur with higher probability. This may explain the formation of the homologous series of $C_nH_m^+$ species. However, it does not account for the disappearance of these mass features at impact velocities greater than 16 km s^{-1}. Under such conditions, it is likely that the kinetic energy of the impinging particles is so high that essentially all chemical bonds are broken, generating solely atomic ions rather than molecular fragments. All structural information regarding the chemical composition of the impinging particles may be lost in this velocity regime.

Plasma cloud chemistry produces two types of velocity-dependent clusters. The first type is observed for impact velocities below 10 km s^{-1} and involves addition of neutral carbon atoms and/or CH radicals to the (protonated) anthracene parent ion. The second type produces carbon clusters that can be represented as $[C_nH_m]^+$ where n=2,3,4,...,17 and m=0,1,2,3.

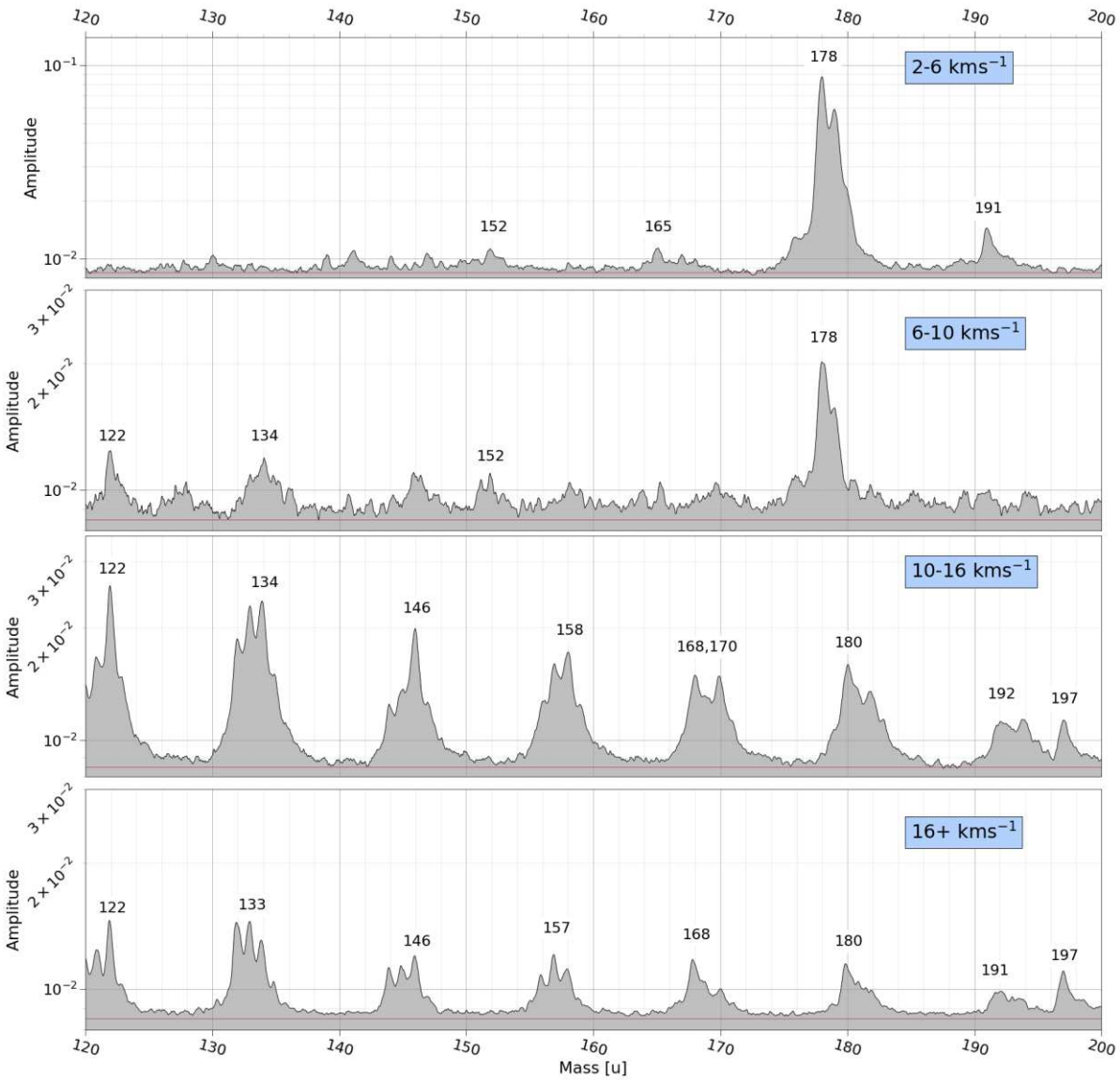

Figure 10. Co-added partial impact ionization spectra recorded for anthracene particles fired at 2 – 6, 6 – 10, 10 – 16, and 16+ km s^{-1} focused on high mass clustering regions (above 150 u).

Inspecting Figure 10, the mass lines observed at 191, 203, and 215 u are representative of mode one clustering; they are assigned to $C14H10^{\cdot+}$ clustered with $CH^{\cdot}$, $C_2H^{\cdot}$, and $C_3H^{\cdot}$, respectively. They could also be representative of protonated anthracene, C14H11+, and C, C_2, or C_3. The higher mass clusters are significantly less abundant due to the decreasing density of $C14H10^{\cdot+}$ and $C14H11^{+}$, which causes fewer collisions to occur. Interestingly, the 191, 203, and 215 u mass lines observed in the 2 – 6 km s^{-1} do not appear in the 6 – 10 km s^{-1} velocity bin. At first sight, it is not clear if this is a genuine result or whether these signals simply lie within the

spectral noise in this case. Thus, we examined a series of narrow velocity bins of width 1 km s^{-1} within the 2 – 10 km s^{-1} range (Fig. 11). In this case, the mass lines at 191, 203, and 215 u are most prominent for velocity bins of 2 – 3, 4 – 5, and 5 – 6 km s^{-1}. For the 3 – 4 km s^{-1} velocity bin, the mass line at 191 u is weak but still discernible, while the 203 u and 215 u features are either absent or lie within the spectral noise. At 6 – 7 km s^{-1}, there is little or no evidence for the 215 u signal and both the 191 u and 203 u mass lines are relatively weak; these latter two features are completely absent at 7 – 8 km s^{-1}. Furthermore, the signal intensity for the parent ion, the protonated parent and the doubly hydrogenated parent ion (mass lines at 178, 179, and 180 u, respectively) is gradually reduced at higher impact velocity in these 'narrow bin' mass spectra and is no longer detected above 9 – 10 km s^{-1}. This pattern indicates that the variation in relative abundance of mode one clusters within the spectra can be attributed to both the availability of carbon and intact anthracene. This is likely due to two factors: there is not sufficient dissociation at impact velocities below 8 km s-1 to have a meaingful density of carbon neutrals/radicals and the issue of particle size. At low velocities, the particles are much more massive than at high veloities due to the nature of dust accelerators. The large, slow particles produce significantly more anthracene ions in proportion to mass than small, fast particles. At velocities below 3 km s^{-1} there is not enough free carbon available to initiate the growth of the clusters. Above 8 km s^{-1}, there is simply insufficient $C_{14}H_{10}^{\cdot+}$ to produce $(C_{14}H_{10}^{\cdot+})(C_nH)$ or $(C_{14}H_{11}^{\cdot+})(C_n)$ clusters.

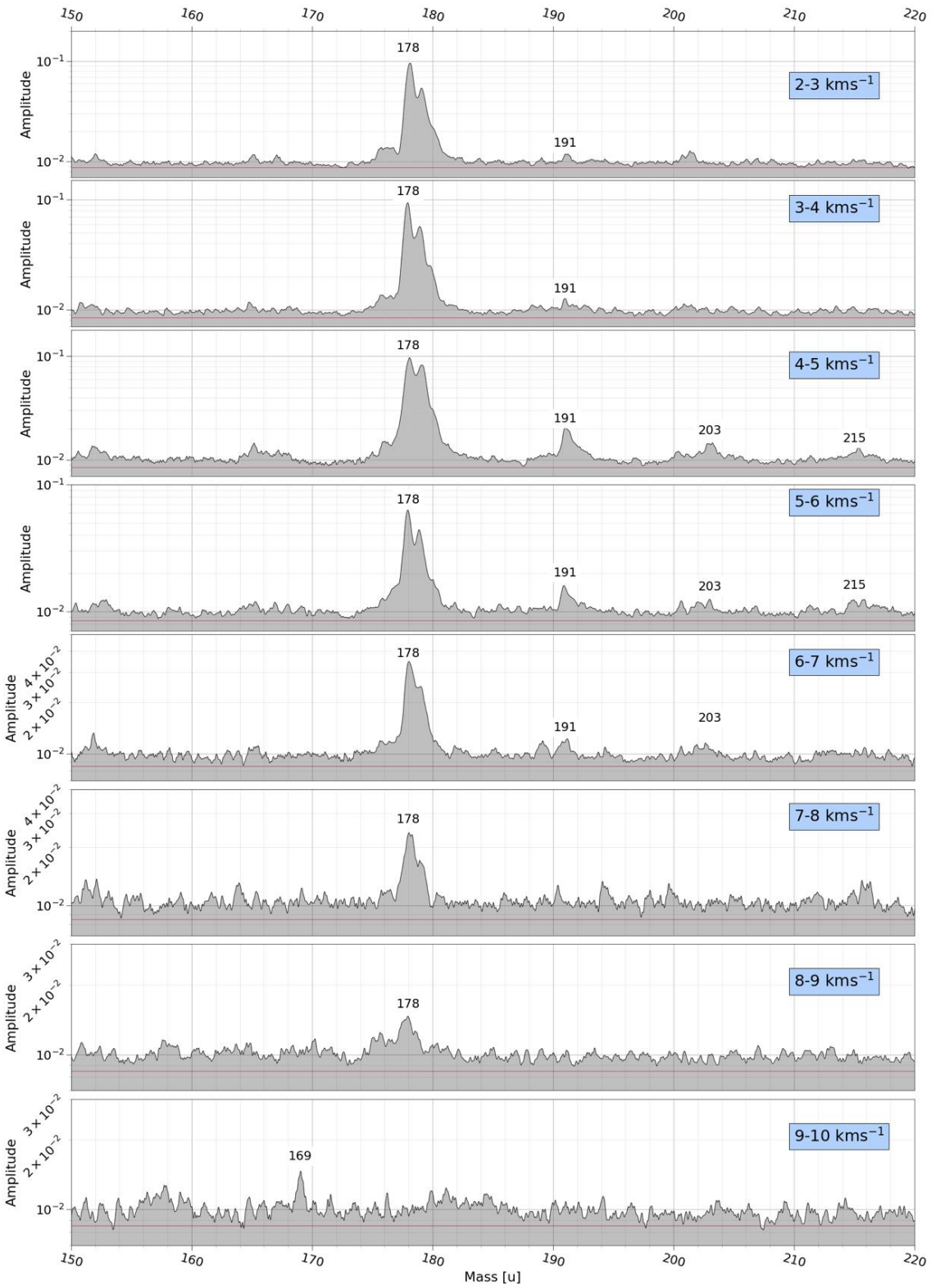

Figure 11. Co-added partial impact ionization spectra recorded for anthracene particles fired at 2 – 3, 3 – 4, 4 – 5, 5 – 6, 6 – 7, 7 – 8, 8 – 9, and 9 – 10 km s^{-1}.

Plasma cloud chemistry also generates a distinctive homologous series of molecular clusters ranging from 36 u up to more than 216 u (Fig. 5) - these are denoted mode two clusters. Such clusters range in size from $C_3H_m^+$ up to $C_{16}H_m^+$ (where m = 0, 1, 2, or 3). Clusters of relatively high mass (e.g., 158, 170, 180, 192, 194, 204, and 216 u) are first observed in the 10 – 16 km s^{-1} velocity bin (Fig. 12). (In addition, there is a mass line at 197 u that is only present at impact velocities above 10 km s^{-1}. However, this feature corresponds to gold ions from the target rather than originating from the anthracene particles). In Figure 11, there is some evidence for such clusters at 9 – 10 km s^{-1} (e.g., the new mass line at 169 u). Again, narrow velocity bins are examined above 9 km s^{-1} to study the effect of varying the impact velocity on the relative abundance of these high mass mode two clusters.

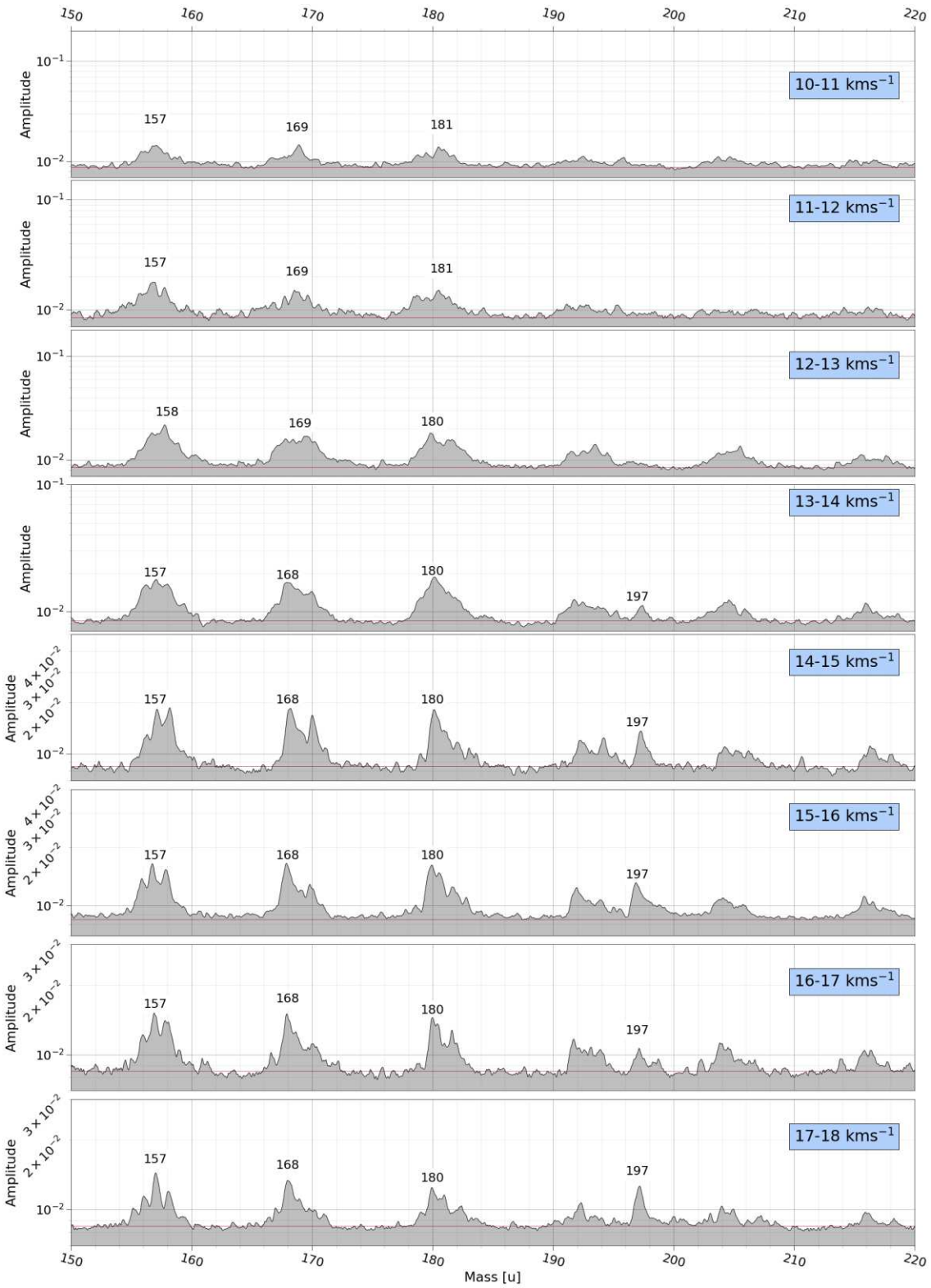

Figure 12. Co-added partial impact ionization spectra recorded for anthracene microparticles fired at 10 to 18 km s^{-1} in 1 km s^{-1} increments.

Such high mass $C_nH_m^+$ clusters are not present at 9 – 10 km s^{-1} but appear at 10 – 11 km s^{-1} (see Figs. 11 and 12). This suggests that there is a lower velocity bound (or minimum kinetic energy) required for their formation. These clusters are particularly prominent between 12 and 15 km s^{-1}. At 17 – 18 km s^{-1}, the mass lines are somewhat weaker but still readily discernible (Fig. 13). Inspecting the highest velocity data set Fig. 13, it is apparent that the upper limit velocity for the formation of $C_nH_m^+$ clusters is approximately 20 km s^{-1}. This is not because of a lack of carbon within the plasma cloud; instead, this building block is now incorporated into lower mass species elsewhere in the spectra.

Although high mass $C_nH_m^+$ clusters are formed up to 20 km s^{-1}, such species do not make a major contribution to the total ion content in high-velocity spectra (> 16 km s^{-1}); this is likely an effect of low S/N of ions produced by these very small, fast particles. Variation in the total % ion content associated with $C_nH_m^+$ (n = 1 – 15 and m = 0,1,2,3) species is examined in Fig. 14, along with the marked increase in CH_m^+ species. For clusters of subsequent numbers of carbon atoms (n = 3, 4 and n = 5, 6 etc.), there is a slight preference towards odd carbon species: on average, odd clusters account for 1.5 ± 0.2% more ion content across the velocity distribution. However, this analysis excludes the ion content associated with $C_nH_m^+$ cations when $m > 3$ as these species either represent molecular fragments or are not consistent with the general patterns observed for $C_nH_m^+$ clusters.

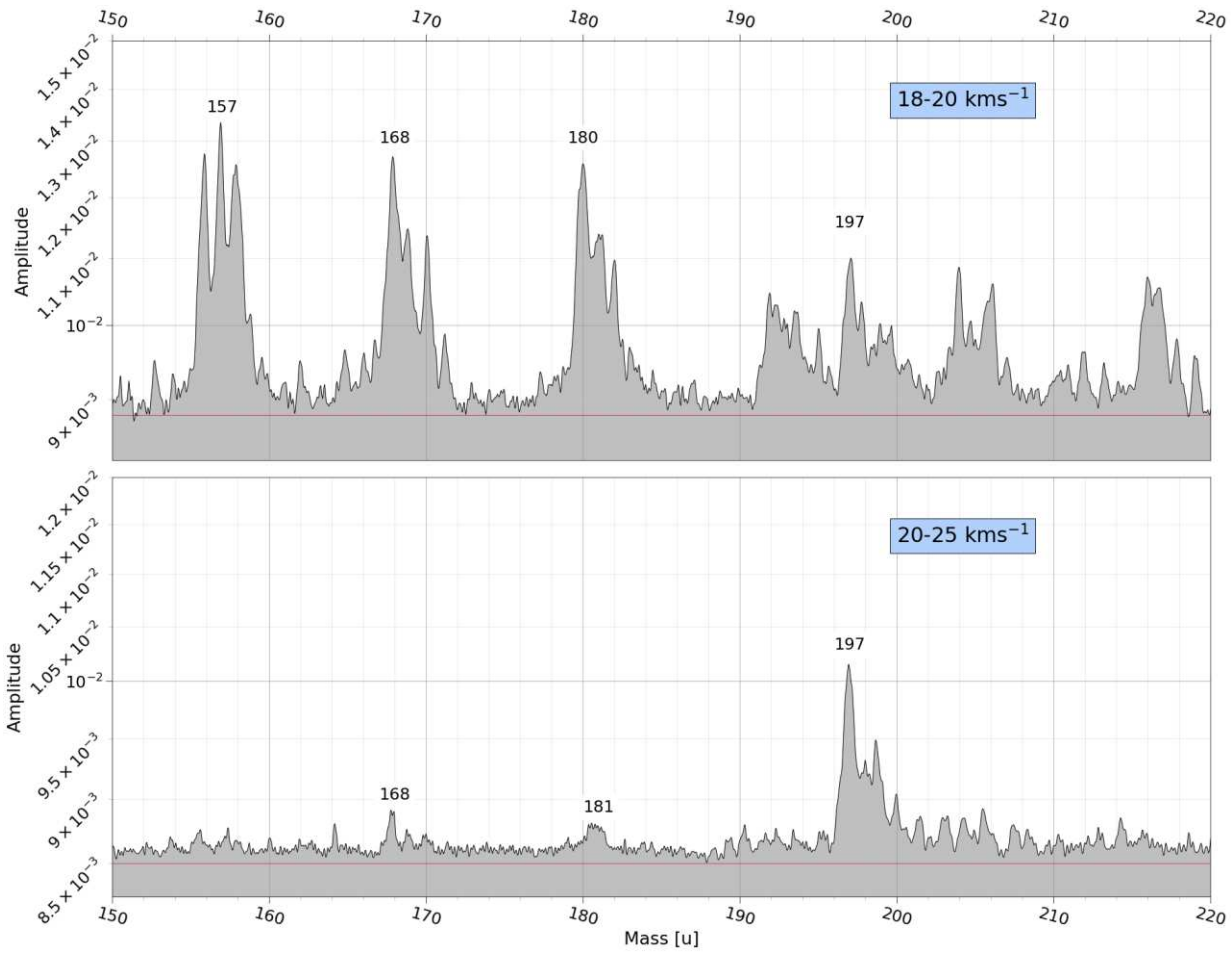

Figure 13. Co-added partial impact ionization spectra recorded for anthracene particles fired at 18 – 20 and 20 – 25 km s^{-1}.

From Figure 14, most of the $C_nH_m^+$ series correspond to $C_2H_m^+$, $C_3H_m^+$ and $C_4H_m^+$ species at low impact velocities (i.e., below 10 km s^{-1}). This is presumably because such species are more likely to collide and react with anthracene radical cations than with each; this is due to the fact that at low speeds, the highest density species is likely anthracene radical cations. This effect is particularly pronounced for the $C_2H_m^+$ species. There is little or no evidence for CH_m^+ within this low-velocity regime, it is likely the CH.+ is colliding and reacting with anthracene and its isomers to form $(C_{14}H_{10})(CH^{\cdot+})$ clusters. This indicates that the preferred fragmentation pathway for the impact ionization of anthracene is similar to that observed for electron ionization; it is the plasma chemistry that produces the majority of the cationic species observed in the anthracene impact ionization mass spectra.

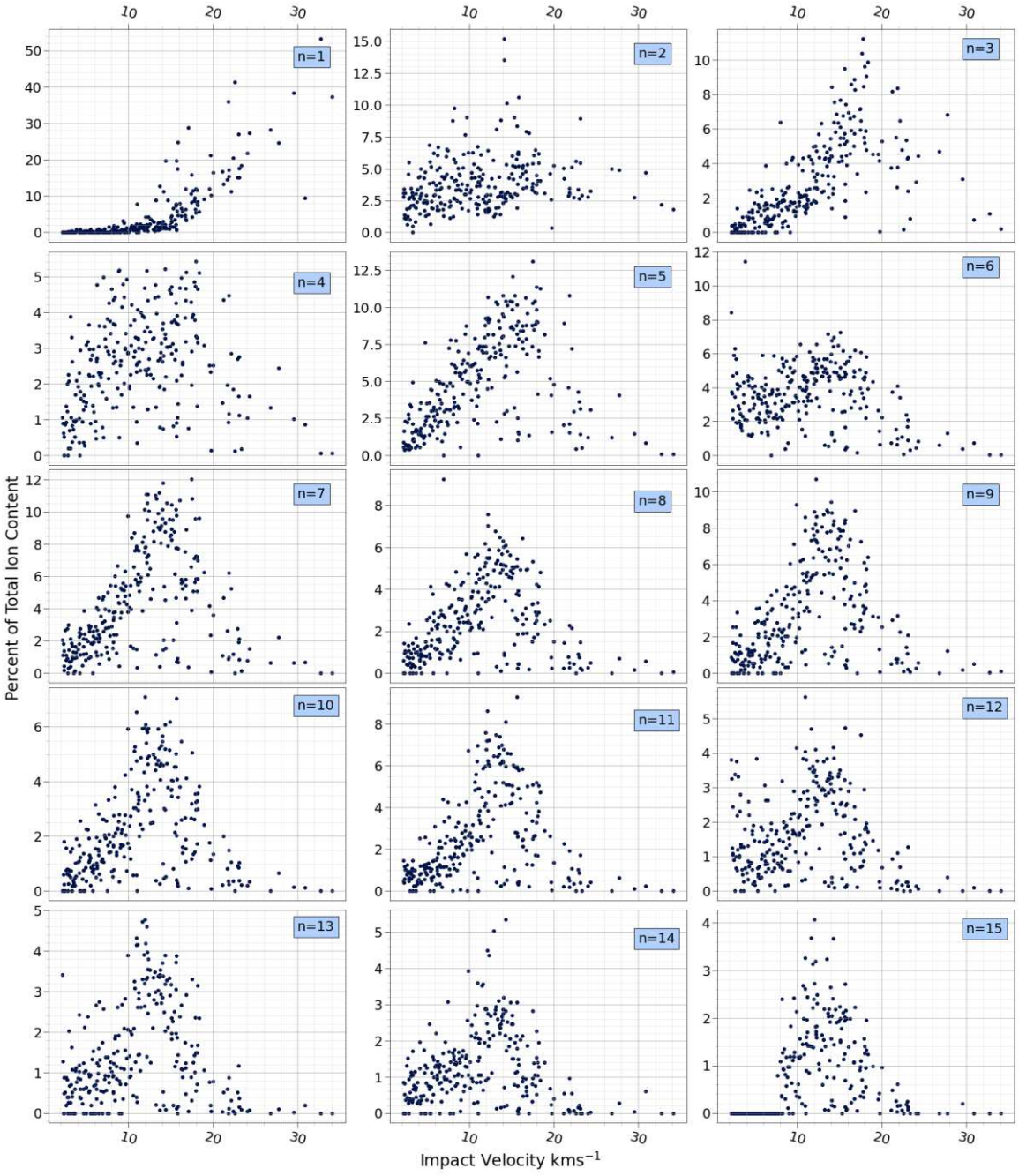

Figure 14. Abundance (represented by the total ion content %) of $C_nH_m^+$ species (where m = 0, 1, 2 or 3) as a function of impact velocity.

Finally, a mass line corresponding to the anthracene dimer is observed at 356 u (Fig. 15). Below 6 km s^{-1}, this species is present in nearly half of the spectra. In contrast, it is present in less than 7% of spectra at 6 – 10 km s^{-1} and is no longer observed at all above 10 km s^{-1} (owing to depletion of the anthracene parent ion within the plasma cloud). When present, the anthracene

dimer has an amplitude that is approximately 18 ± 3 % that of the anthracene parent ion. This calculation excludes the spectra in which the anthracene dimer is not sufficiently large when compared to the noise floor.

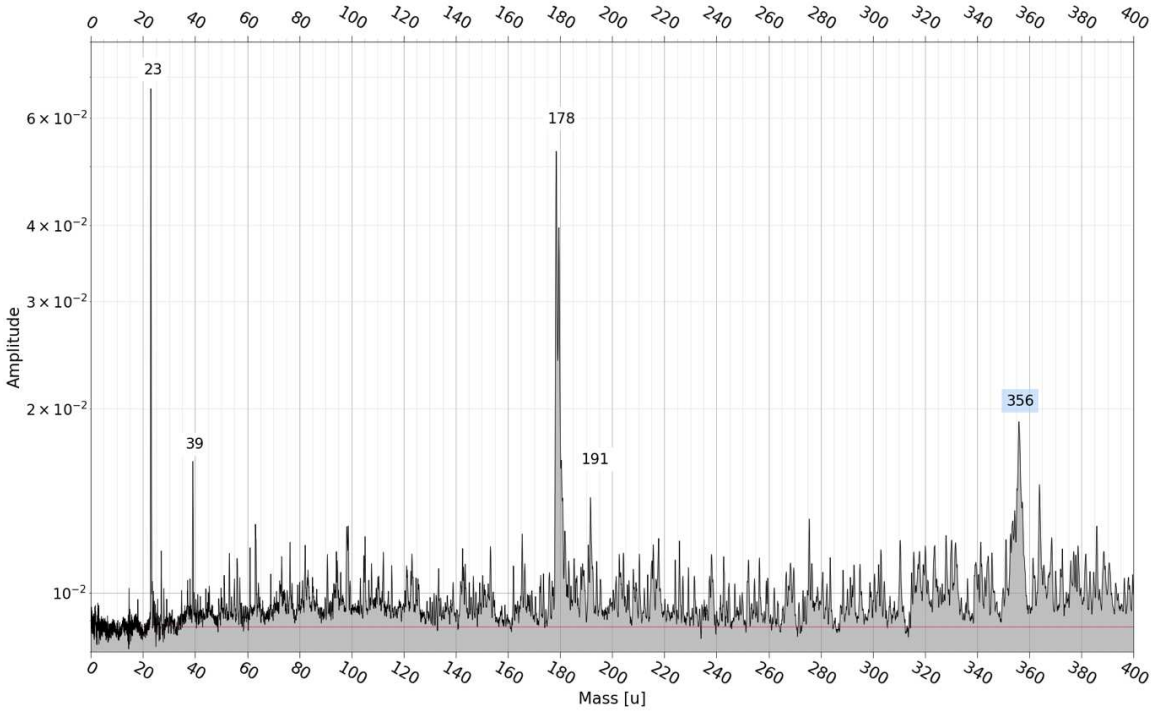

Figure 15. Impact ionization mass spectrum recorded at 3 km s^{-1} confirming the presence of anthracene dimer (mass 356 u) as well as other characteristic features (such as K^+ and the 191 u mode one cluster) of the low-velocity bin (2 – 6 km s^{-1}).

Identification of $C_{14}H_{10}^{\cdot+}$ at Various Impact Velocities

The TOF mass spectra generated by impact ionization vary as a function of impact velocity. Individual high-velocity spectra (> 16 km s^{-1}) consistently exhibit intense H signals (primarily H^+ and H_2^+) as well as C^+ (12 u) and C_2^+ (24 u) features but otherwise display only mode two carbon-rich clusters and their singly protonated species, as well as the $C_{14}H_{12}^{\cdot+}$ and $C_{14}H_{13}^+$ species. The 10 – 16 km s^{-1} velocity bin produces mass spectra that contain a 56 u mass line tentatively assigned to $C_3H_5NH^+$ originating from the PPy overlayer, as well as mode two clusters. This latter feature would not be expected in mass spectra recorded for PAH-based dust grains during future space missions. An H^+ signal also appears in this velocity bin, but it is not a major contributor. Mass spectra recorded for impact ionization events at 6 – 10 km s^{-1} exhibit

relatively little C^+ and $C_3H_5NH^+$. Instead, the parent ion mass and its protonated counterpart, $C_{14}H_{10}^+$ (178 u) and $C_{14}H_{11}^+$ (179 u), now make a significant contribution to the overall ion content. Low-velocity spectra recorded at 2 – 6 km s^{-1} are primarily composed of the same two species as well mass lines assigned to Na^+, Ca^+ and K^+. Spectra below 8 km s^{-1} also show significant $C_{14}H_{10}^{\cdot+}$ CH clusters, as discussed above.

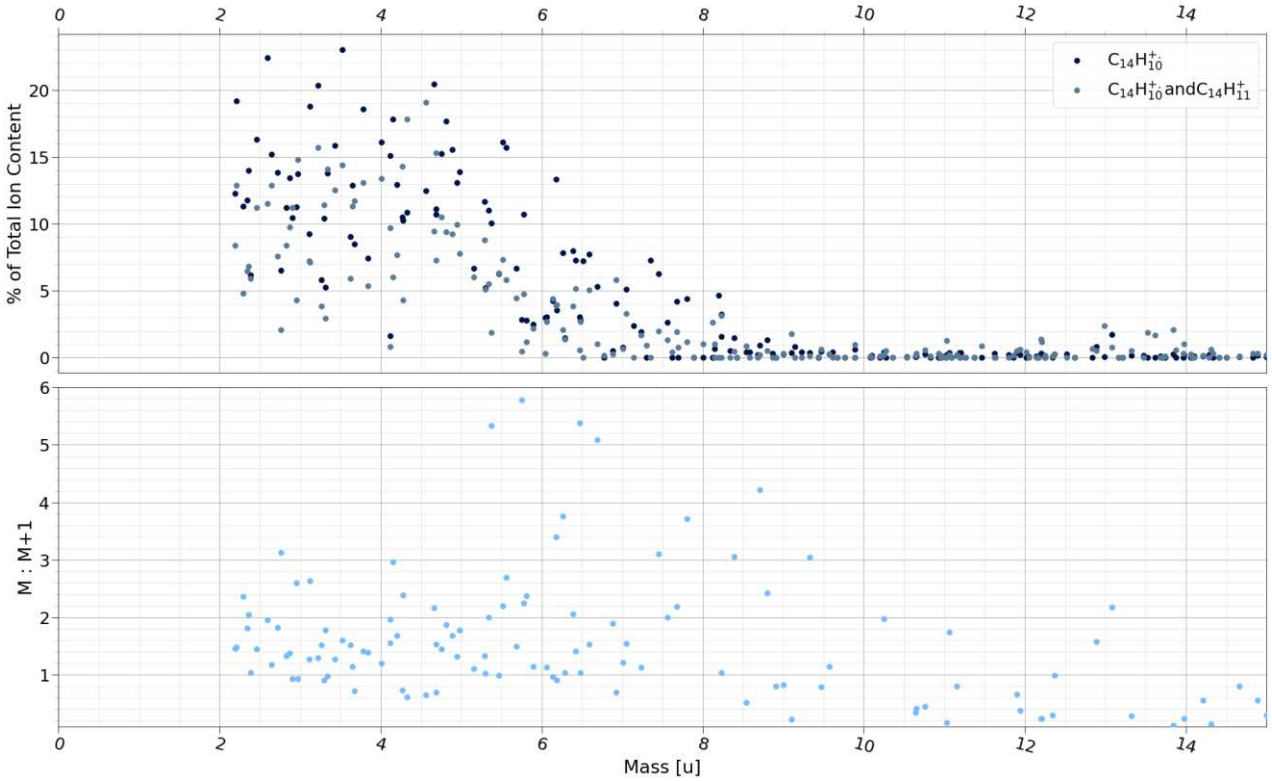

Figure 16. (a) $C_{14}H_{10}^{\cdot+}$ (M) and protonated species (M+1) detectability as a function of impact velocity. (b) M:M+1 atomic ratio as a function of impact velocity.

Although identified over a wide range of velocities, the $C_{14}H_{10}^{\cdot+}$ radical cation only contributes a significant portion (>1.5%) of the total ion content of any given spectrum at impact velocities below 8 km s^{-1} (Fig. 16). Above this threshold value, the extent of molecular fragmentation is too great to observe this species. In many cases, the most prominent cation observed in the impact ionization mass spectrometry of organic molecules is the M+1 species [*Klenner et al.* 2020]. This is also true of the anthracene impact ionization mass spectra (Fig. 16). In the context of the present study, this enables identification of the parent ion, which is likely to be useful for the interpretation of impact ionization data obtained during future space missions.

It is important to characterize the optimal velocity at which anthracene can be identified. The lack of identifiable species at m/z 178 and 179, the presence of multiple identifying clusters such as $(C_{14}H_{10})(CH)^+$ and $(C_{14}H_{11})(C_2H)^+$, and the presence of the anthracene dimer make the optimal velocity range for detection and identification of anthracene 4 – 5 km s^{-1}. The features seen at velocities of upwards of ~8 km s-1 are still indicative of a hydrocarbon species rather than a metal or mineral; this is important information as we learn more about the impact ionization behavior of PAHs.

Conclusions

The dust accelerator experiments reported herein demonstrate that the ionization of complex organic dust particles such as anthracene is strongly dependent on the impact velocity. The TOF mass spectra recorded for anthracene-derived ionic plasmas can be organized into four velocity bins: low (2 – 6 km s^{-1}), mid-low (6 – 10 km s^{-1}), mid-high (10 – 16 km s^{-1}), and high velocity (16+ km s^{-1}). Each of these bins exhibits good repeatability from impact to impact and is characterized by distinct fragmentation and/or cluster patterns compared to spectra recorded for the other bins. The 2 – 6 km s^{-1} bin is characterized by the anthracene parent cation, protonated species, and $(C_{14}H_{10})(CH)^+$ and $(C_{14}H_{10})(C_2H)^+$) clusters plus easily ionizable contaminants such as sodium. The spectra obtained for the 6 – 10 km s^{-1} bin are similar to those in the 2 – 6 km s^{-1} bin but the parent ions (M) and M+1 are increasingly depleted at higher velocity. It is difficult to know whether this effect is because large particles always travel more slowly compared to small particles in dust accelerator experiments. In contrast, even relatively massive particles can move at high velocities in deep space (e.g. interstellar dust grains). Finally, the spectra recorded for the 16+ km s^{-1} bin contain no parent ion, relatively few mid-mass species, high amplitude features associated with H^+ and C^+, and low mass mode two clusters. Importantly, none of the above spectral features correlate with the 70 eV electron ionization mass spectrum reported for anthracene due to the plasma chemistry effects inherent to dust impact ionization. Further work is required to understand the complex impact ionization behavior exhibited by polycyclic aromatic hydrocarbons.

Regarding *in situ* detection of PAH dust grains using next-generation dust impact ionization instruments, our findings should inform both fundamental instrument design

principles and detection/environmental requirements. One important finding is that dust impact ionization instruments must be capable of achieving a mass resolution of 1 u at relatively high masses (at least 200 u) to reliably identify features such as protonated PAH parent ion and mode one clusters. Most importantly, the anthracene parent molecule cannot be detected above 10 km s^{-1} in our experiments. This suggests that the identification of interplanetary and interstellar PAHs will be a formidable technical challenge. Nevertheless, the $C_{14}H_{10}^{\cdot+}$ ion is readily identified within ionic plasma generated from impact ionization events below 10 km s^{-1}. In addition to the $C_{14}H_{10}^{\cdot+}$ and $C_{14}H_{11}^{+}$ cations, distinctive fragments such as $C_2H_2^{+}$ (26 u) and $C_2H_4^{+}$ (28 u), mode one clusters characteristic of anthracene at 191 u and 203 u, and the presence of anthracene dimer (356 u) are observed under such conditions.

Acknowledgments

This work was supported by NASA's IMAP Instrument, and in part by NASA's Solar System Exploration Research Virtual Institute (SSERVI) Cooperative Agreement Notice, Grant 80NSSC19M0217.

S.P.A. acknowledges an EPSRC *Established Career* Particle Technology Fellowship (EP/R003009/1). S.P.A. also wishes to thank the Leverhulme Trust for postdoctoral support of D.H.H.C. (RPG-2022-260).

References

Anthracene. NIST Chemistry WebBook, SRD 69. National Institute of Standards and Technology. N.d. webbook.nist.gov/cgi/cbook.cgi?ID=C120127&Mask=200#Mass-Spec.(accessed 2021-07-01).(NIST MS number: 228201).

Burchell, M. J., & Armes, S. P. Impact ionisation spectra from hypervelocity impacts using aliphatic poly (methyl methacrylate) microparticle projectiles. Rapid Communications in Mass Spectrometry, ***2011****, 25(4), 543-550. https://doi.org/10.1002/rcm.4887*

Chan, D. H., Millet, A.. Fisher, C. R., Price, M. C., Burchell, M. J. and Armes, S. P. Synthesis and Characterization of Polypyrrole-Coated Anthracene Microparticles: A New Synthetic Mimic for Polyaromatic Hydrocarbon-Based Cosmic Dust. ACS Applied Materials & Interfaces ***2021,*** *13 (2), 3175-3185. https://doi.org/10.1021/acsami.0c19758*

Chiang, Y. K., & Ménard, B. Extragalactic imprints in galactic dust maps. The Astrophysical Journal, ***2019****, 870(2), 120. https://doi.org/10.3847/1538-4357/aaf4f6*

Clemett, S. J., Sandford, S. A., NAKAMURA-MESSENGER, K., Hoerz, F., & McKAY, D. S. Complex aromatic hydrocarbons in Stardust samples collected from comet 81P/Wild 2. Meteoritics & Planetary Science, ***2010****, 45(5), 701-722. https://doi.org/10.1111/j.1945-5100.2010.01062.x*

Fiege, K., Trieloff, M., Hillier, J. K., Guglielmino, M., Postberg, F., Srama, R., ... & Blum, J. Calibration of relative sensitivity factors for impact ionization detectors with high-velocity silicate microparticles. Icarus, ***2014,*** *241, 336-345. http://dx.doi.org/10.1016%2Fj.icarus.2014.07.015*

Goldsworthy, B. J., Burchell, M. J., Cole, M. J., Green, S. F., Leese, M. R., McBride, N., ... & Khan, M. A. Laboratory calibration of the cassini cosmic dust analyser (CDA) using new, low density projectiles. Advances in Space Research, ***2002****, 29(8), 1139-1144. https://doi.org/10.1016/S0273-1177(02)00129-1*

Goldsworthy, B. J., Burchell, M. J., Cole, M. J., Armes, S. P., Khan, M. A., Lascelles, S. F., ... & Bigger, S. W. Time of flight mass spectra of ions in plasmas produced by hypervelocity impacts of organic and mineralogical microparticles on a cosmic dust analyser. Astronomy & Astrophysics, ***2003****, 409(3), 1151-1167 https://doi.org/10.1051/0004-6361:20031087*

Grün, E., Srama, R., Krüger, H., Kempf, S., Dikarev, V., Helfert, S. and Moragas-Klostermeyer, G. 2002 Kuiper prize lecture: dust astronomy. Icarus, ***2005****, 174(1), pp.1-14. https://doi.org/10.1016/j.icarus.2004.09.010*

Hillier, J. K., Sestak, S., Green, S. F., Postberg, F., Srama, R., & Trieloff, M. The production of platinum-coated silicate nanoparticle aggregates for use in hypervelocity impact experiments. Planetary and Space Science, ***2009****, 57(14-15), 2081-2086. https://doi.org/10.1016/j.pss.2009.09.019*

Hillier, J. K., F. Postberg, S. Sestak, R. Srama, S. Kempf, M. Trieloff, Z. Sternovsky, and S. F. Green. Impact ionization mass spectra of anorthite cosmic dust analogue particles, J. Geophys. Res., ***2012****, 117, E09002, https://doi.org/10.1029/2012JE004077.*

Hillier, J. K., K. Fiege, M. Trieloff, and R. Srama. Numerical modelling of mineral impact ionisation spectra. Planetary and Space Science 89, ***2013*** *159–166 (2013), https://doi.org/10.1016/j.pss.2013.08.016*

Hillier, J. K., Sternovsky, Z., Kempf, S., Trieloff, M., Guglielmino, M., Postberg, F., & Price, M. C. Impact ionisation mass spectrometry of platinum-coated olivine and magnesite-dominated cosmic dust analogues. Planetary and Space Science, ***2018****, 156, 96-110. https://doi.org/10.1016/j.pss.2017.10.002*

Hrodmarsson, H. R., Bouwman, J., Tielens, A. G., & Linnartz, H. Similarities and dissimilarities in the fragmentation of polycyclic aromatic hydrocarbon cations: A case study involving three dibenzopyrene isomers. International Journal of Mass Spectrometry, ***2022****, 476, 116834. https://doi.org/10.1016/j.ijms.2022.116834*

Hrodmarsson, H. R., Bouwman, J., Tielens, A. G., & Linnartz, H. Fragmentation of the PAH cations of Isoviolanthrene and Dicoronylene: A case made for interstellar cyclo [n] carbons as products of universal fragmentation processes. International Journal of Mass Spectrometry, ***2023****, 485, 116996. https://doi.org/10.1016/j.ijms.2022.116996*

Keifer, D. Z., Pierson, E. E., & Jarrold, M. F. Charge detection mass spectrometry: weighing heavier things. Analyst, ***2017****, 142(10), 1654-1671.*

Khawaja, N., Hillier, J., Klenner, F., Nölle, L., Zou, Z., Napoleoni, M., ... & Postberg, F. Complementary mass spectral analysis of isomeric O-bearing organic compounds and fragmentation differences through analog techniques for spaceborne mass spectrometers. The Planetary Science Journal, ***2022****, 3(11), 254.*

Klenner, F., Postberg, F., Hillier, J., Khawaja, N., Reviol, R., Stolz, F., ... & Nölle, L. Analog experiments for the identification of trace biosignatures in ice grains from extraterrestrial ocean worlds. Astrobiology, ***2020****, 20(2), 179-189.* https://doi.org/10.1089/ast.2019.2065

Leger, A., & Puget, J. Identification of the 'unidentified' IR emission features of interstellar dust. Astronomy and Astrophysics (ISSN 0004-6361), ***1984****, vol. 137, no. 1, p. L5-L8., 137, L5-L8.*

Li, A., & Draine, B. T. Infrared emission from interstellar dust. II. The diffuse interstellar medium. The Astrophysical Journal, ***2001****, 554(2), 778.* 10.48550/arXiv.astro-ph/0011319

McComas, D. J., Christian, E. R., Schwadron, N. A., Fox, N., Westlake, J., Allegrini, F., ... & Zirnstein, E. J. Interstellar mapping and acceleration probe (IMAP): A new NASA mission. Space science reviews, ***2018****, 214, 1-54.* https://doi.org/10.1007/s11214-018-0550-1.

Mocker, A., Bugiel, S., Auer, S., Baust, G., Colette, A., Drake, K., ... & Srama, R. A 2 MV Van de Graaff accelerator as a tool for planetary and impact physics research. Review of Scientific Instruments, ***2011****, 82(9).* https://doi.org/10.1063/1.3637461

Ozaki, N., Yamamoto, T., Gonzalez-Franquesa, F., Gutierrez-Ramon, R., Pushparaj, N., Chikazawa, T., ... & Takashima, T. Mission design of DESTINY+: Toward active asteroid (3200) Phaethon and multiple small bodies. Acta Astronautica, ***2022****, 196, 42-56.* https://doi.org/10.1016/j.actaastro.2022.03.029

Postberg, F., Kempf, S., Rost, D., Stephan, T., Srama, R., Trieloff, M., ... & Goerlich, M. Discriminating contamination from particle components in spectra of Cassini's dust detector CDA. Planetary and Space Science, ***2009****, 57(12), 1359-1374.* https://doi.org/10.1016/j.pss.2009.06.027

Rachev, Mikhail, Ralf Srama, Andre Srowig, and Eberhard Grün. "Large Area Mass Analyzer." Nuclear Instruments and Methods in Physics Research Section A: Accelerators, Spectrometers, Detectors and Associated Equipment, ***2004****, 535 (1–2): 162–64.* https://doi.org/10.1016/j.nima.2004.07.121.

*Raman V, V., Roy, A., Sivaraman, B., Ganesh, S., and Mason, N.: Tentative detection of vibrationally excited Polycyclic Aromatic Hydrocarbons in Comets, Europlanet Science Congress **2020**, online, 21 September–9 Oct 2020, EPSC2020-1072. https://doi.org/10.5194/epsc2020-1072.*

*Sales, D. A., Pastoriza, M. G., & Riffel, R. Polycyclic aromatic hydrocarbon and emission line ratios in active galactic nuclei and starburst galaxies. The Astrophysical Journal, **2010**, 725(1), 605. https://doi.org/10.1088/0004-637X/725/1/605*

*Seok, J. Y., & Li, A. Polycyclic aromatic hydrocarbons in protoplanetary disks around Herbig Ae/Be and T Tauri stars. The Astrophysical Journal, **2017**, 835(2), 291. http://dx.doi.org/10.3847/1538-4357/835/2/291*

*Shu, A., Collette, A., Drake, K., Grün, E., Horányi, M., Kempf, S., ... & Thomas, E. 3 MV hypervelocity dust accelerator at the Colorado Center for Lunar Dust and Atmospheric Studies. Review of Scientific Instruments, **2012**, 83(7). https://doi.org/10.1063/1.4732820*

*Srama, R., Ahrens, T. J., Altobelli, N., Auer, S., Bradley, J. G., Burton, M., ... & Zook, H. A. The Cassini cosmic dust analyzer. Space Science Reviews, **2004**, 114, 465-518. https://doi.org/10.1007/s11214-004-1435-z*

*Srama, R., A. Srowig, M. Rachev, E. Grün, S. Kempf, G. Moragas-Klostermeyer, T. Conlon, D. Harris, S. Auer, A. Glasmachers, S. Helfert, H. Linnemann, and V. Tschernjawski, "Development of an advanced dust telescope," Earth Moon and Planets, **2005**, vol. 95, pp. 211–220, https://doi.org/10.1007/s11038-005-9040-z.*

*Srama, R., Woiwode, W., Postberg, F., Armes, S. P., Fujii, S., Dupin, D., ... & Grün, E. Mass spectrometry of hyper-velocity impacts of organic micrograins. Rapid Communications in Mass Spectrometry: An International Journal Devoted to the Rapid Dissemination of Up-to-the-Minute Research in Mass Spectrometry, **2009**, 23(24), 3895-3906. https://doi.org/10.1002/rcm.4318*

Sternovsky, Z, K Amyx, G Bano, M Landgraf, M Horányi, S Knappmiller, S Robertson, E Grün, R Srama, and Siegfried Auer. "Large Area Mass Analyzer Instrument for the

Chemical Analysis of Interstellar Dust Particles." Review of Scientific Instruments 78 (1): ***2007****, 014501–10. https://doi.org/10.1063/1.2431089.*

Sternovsky, Zoltán, Eberhard Grün, Keith Drake, Jianfeng Xie, Mihály Horányi, Ralf Srama, Sascha Kempf, et al. "Novel Instrument for Dust Astronomy: Dust Telescope." In, 1–8. ***2011*** *Aerospace Conference. 2011 Aerospace Conference. https://doi.org/10.1109/aero.2011.5747300.*

Sternovsky, Z, A J Gemer, E Grün, M Horányi, S Kempf, K Maute, F Postberg, R Srama, and E Williams. 2015. "Hyperdust: An Advanced in-Situ Detection and Chemical Analysis of Microparticles in Space." In, 1–10. 2015 IEEE Aerospace Conference. ***2015*** *IEEE Aerospace Conference. https://doi.org/10.1109/aero.2015.7119085.*

Tielens, A. G. Interstellar polycyclic aromatic hydrocarbon molecules. Annu. Rev. Astron. Astrophys., ***2008****, 46, 289-337.* https://doi.org/10.1146/annurev.astro.46.060407.145211

Thomas, Evan, Siegfried Auer, Keith Drake, Mihály Horányi, Tobin Munsat, and Anthony Shu. "FPGA Cross-Correlation Filters for Real-Time Dust Detection and Selection." Planetary and Space Science 89: ***2013****, 71–76. https://doi.org/10.1016/j.pss.2013.09.004.*

West, B., Sit, A., Mohamed, S., Joblin, C., Blanchet, V., Bodi, A., & Mayer, P. M. Dissociation of the anthracene radical cation: a comparative look at iPEPICO and collision-induced dissociation mass spectrometry results. The Journal of Physical Chemistry A, ***2014****, 118(42), 9870-9878. https://doi.org/10.1021/jp505438f*

Woo, J. H., Kim, J. H., Imanishi, M., & Park, D. The Connection between 3.3 μm Polycyclic Aromatic Hydrocarbon Emission and Active Galactic Nucleus Activity. The Astronomical Journal, ***2012****, 143(2), 49. https://doi.org/10.1088/0004-6256/143/2/49*

Xiao, X., Chen, Z. & Chen, B. H/C atomic ratio as a smart linkage between pyrolytic temperatures, aromatic clusters and sorption properties of biochars derived from diverse precursory materials. Sci Rep 6, ***2016****, 22644. https://doi.org/10.1038/srep22644*

Zhao, L., Kaiser, R. I., Xu, B., Ablikim, U., Ahmed, M., Evseev, M. M., ... & Mebel, A. M. Low-temperature formation of polycyclic aromatic hydrocarbons in Titan's atmosphere. Nature Astronomy, ***2018****, 2(12), 973-979.. https://doi.org/10.1038/s41550-018-0585-y*